



**HAL**  
open science

## Photometry of the Didymos System across the DART Impact Apparition

Nicholas Moskovitz, Cristina Thomas, Petr Pravec, Tim Lister, Tom Polakis, David Osip, Theodore Kareta, Agata Rožek, Steven R. Chesley, Shantanu P. Naidu, et al.

► **To cite this version:**

Nicholas Moskovitz, Cristina Thomas, Petr Pravec, Tim Lister, Tom Polakis, et al.. Photometry of the Didymos System across the DART Impact Apparition. *The Planetary Science Journal*, 2024, 5, 10.3847/PSJ/ad0e74 . insu-04853477

**HAL Id: insu-04853477**

**<https://insu.hal.science/insu-04853477v1>**

Submitted on 23 Dec 2024

**HAL** is a multi-disciplinary open access archive for the deposit and dissemination of scientific research documents, whether they are published or not. The documents may come from teaching and research institutions in France or abroad, or from public or private research centers.

L'archive ouverte pluridisciplinaire **HAL**, est destinée au dépôt et à la diffusion de documents scientifiques de niveau recherche, publiés ou non, émanant des établissements d'enseignement et de recherche français ou étrangers, des laboratoires publics ou privés.



Distributed under a Creative Commons Attribution 4.0 International License



# Photometry of the Didymos System across the DART Impact Apparition

Nicholas Moskovitz<sup>1</sup>, Cristina Thomas<sup>2</sup>, Petr Pravec<sup>3</sup>, Tim Lister<sup>4</sup>, Tom Polakis<sup>1</sup>, David Osip<sup>5</sup>, Theodore Karetka<sup>1</sup>, Agata Rożek<sup>6</sup>, Steven R. Chesley<sup>7</sup>, Shantanu P. Naidu<sup>7</sup>, Peter Scheirich<sup>3</sup>, William Ryan<sup>8</sup>, Eileen Ryan<sup>8</sup>, Brian Skiff<sup>1</sup>, Colin Snodgrass<sup>6</sup>, Matthew M. Knight<sup>9</sup>, Andrew S. Rivkin<sup>10</sup>, Nancy L. Chabot<sup>10</sup>, Vova Ayvazian<sup>11</sup>, Irina Belskaya<sup>12,13</sup>, Zouhair Benkhaldoun<sup>14</sup>, Daniel N. Berteșteanu<sup>15</sup>, Mariangela Bonavita<sup>6</sup>, Terrence H. Bressi<sup>16</sup>, Melissa J. Brucker<sup>16</sup>, Martin J. Burgdorf<sup>17</sup>, Otabek Burkhonov<sup>18</sup>, Brian Burt<sup>1</sup>, Carlos Contreras<sup>5</sup>, Joseph Chatelain<sup>4</sup>, Young-Jun Choi<sup>19,20</sup>, Matthew Daily<sup>4</sup>, Julia de León<sup>21</sup>, Kamoliddin Ergashev<sup>18</sup>, Tony Farnham<sup>22</sup>, Petr Fatka<sup>3</sup>, Marin Ferrais<sup>23</sup>, Stefan Geier<sup>24,25</sup>, Edward Gomez<sup>4,26</sup>, Sarah Greenstreet<sup>27</sup>, Hannes Gröller<sup>16</sup>, Carl Hergenrother<sup>28</sup>, Carrie Holt<sup>22</sup>, Kamil Hornoch<sup>3</sup>, Marek Husárik<sup>29</sup>, Raguli Inasaridze<sup>11,30</sup>, Emmanuel Jehin<sup>31</sup>, Elahe Khalouei<sup>32</sup>, Jean-Baptiste Kikwaya Eluo<sup>33</sup>, Myung-Jin Kim<sup>19</sup>, Yuriy Krugly<sup>13,34</sup>, Hana Kučáková<sup>3</sup>, Peter Kušnirák<sup>3</sup>, Jeffrey A. Larsen<sup>35</sup>, Hee-Jae Lee<sup>19</sup>, Cassandra Lejoly<sup>16</sup>, Javier Licandro<sup>21</sup>, Penélope Longa-Peña<sup>36</sup>, Ronald A. Mastaler<sup>16</sup>, Curtis McCully<sup>4</sup>, Hong-Kyu Moon<sup>19</sup>, Nidia Morrell<sup>5</sup>, Arushi Nath<sup>37</sup>, Dagmara Oszkiewicz<sup>34</sup>, Daniel Parrott<sup>38</sup>, Liz Phillips<sup>4,39</sup>, Marcel M. Popescu<sup>40</sup>, Donald Pray<sup>41</sup>, George Pantelimon Prodan<sup>40</sup>, Markus Rabus<sup>42</sup>, Michael T. Read<sup>16</sup>, Inna Reva<sup>43</sup>, Vernon Roark<sup>44</sup>, Toni Santana-Ros<sup>45,46</sup>, James V. Scotti<sup>16</sup>, Taiyo Tataru<sup>35</sup>, Audrey Thirouin<sup>1</sup>, David Tholen<sup>44</sup>, Volodymyr Troianskyi<sup>34,47,48</sup>, Andrew F. Tubbiolo<sup>16</sup>, and Katelyn Villa<sup>9</sup>

<sup>1</sup> Lowell Observatory, 1400 West Mars Hill Road, Flagstaff, AZ 86004, USA; [nmosko@lowell.edu](mailto:nmosko@lowell.edu)

<sup>2</sup> Northern Arizona University, USA

<sup>3</sup> Astronomical Institute of the Academy of Sciences of the Czech Republic, Fričova 298, Ondřejov, CZ-25165, Czech Republic

<sup>4</sup> Las Cumbres Observatory, Goleta, CA, USA

<sup>5</sup> Las Campanas Observatory, Chile

<sup>6</sup> Institute for Astronomy, University of Edinburgh, Royal Observatory, Edinburgh, EH9 3HJ, UK

<sup>7</sup> Jet Propulsion Laboratory, California Institute of Technology, Pasadena, CA, USA

<sup>8</sup> New Mexico Institute of Mining and Technology/Magdalena Ridge Observatory, 801 Leroy Place, Socorro, NM 87801, USA

<sup>9</sup> Physics Department, United States Naval Academy, 572C Holloway Road, Annapolis, MD 21402, USA

<sup>10</sup> Johns Hopkins University Applied Physics Laboratory, USA

<sup>11</sup> E. Kharadze Georgian National Astrophysical Observatory, Abastumani, Georgia

<sup>12</sup> LESIA, Observatoire de Paris, Université PSL, CNRS, Université Paris Cité, Sorbonne Université, Meudon, France

<sup>13</sup> Institute of Astronomy, V.N. Karazin Kharkiv National University, Kharkiv, Ukraine

<sup>14</sup> Oukaïmeden Observatory, High Energy Physics and Astrophysics Laboratory, Cadi Ayyad University, BP 2390, Marrakech, Morocco

<sup>15</sup> Astronomical Institute of the Romanian Academy, Romania

<sup>16</sup> LPL/UA, USA

<sup>17</sup> Universität Hamburg, Faculty of Mathematics, Informatics and Natural Sciences, Department of Earth Sciences, Meteorological Institute, Bundesstraße 55, D-20146 Hamburg, Germany

<sup>18</sup> Ulugh Beg Astronomical Institute, Tashkent, Uzbekistan

<sup>19</sup> Korea Astronomy and Space Science Institute, 776, Daedeokdae-ro, Yuseong-gu, Daejeon 34055, Republic of Korea

<sup>20</sup> University of Science and Technology, 217, Gajeong-ro, Yuseong-gu, Daejeon 34113, Republic of Korea

<sup>21</sup> Instituto de Astrofísica de Canarias, Spain

<sup>22</sup> University of Maryland, USA

<sup>23</sup> Florida Space Institute, University of Central Florida, 12354 Research Parkway, Orlando, FL 32826, USA

<sup>24</sup> Gran Telescopio Canarias (GRANTECAN), Cuesta de San José s/n, E-38712, Breña Baja, La Palma, Spain

<sup>25</sup> Instituto de Astrofísica de Canarias, Vía Láctea s/n, E-38200, La Laguna, Tenerife, Spain

<sup>26</sup> School of Physics and Astronomy, Cardiff University, Queens Buildings, The Parade, Cardiff CF24 3AA, UK

<sup>27</sup> DiRAC Institute and the Department of Astronomy, University of Washington, USA

<sup>28</sup> Ascending Node Technologies, LLC, Tucson, AZ, USA

<sup>29</sup> Astronomical Institute of the Slovak Academy of Sciences, 059 60 Tatranská Lomnica, The Slovak Republic

<sup>30</sup> Samtskhe-Javakheti State University, Akhaltsikhe, Georgia

<sup>31</sup> Space sciences, Technologies & Astrophysics Research (STAR) Institute, University of Liège, Belgium

<sup>32</sup> Astronomy Research Center, Research Institute of Basic Sciences, Seoul National University, 1 Gwanak-ro, Gwanak-gu, Seoul 08826, Republic of Korea

<sup>33</sup> Vatican Observatory, V-00120 Vatican City State, Italy

<sup>34</sup> Astronomical Observatory Institute, Faculty of Physics, Adam Mickiewicz University, Słoneczna 36, 60-286 Poznań, Poland

<sup>35</sup> USNA, USA

<sup>36</sup> Centro de Astronomía, Universidad de Antofagasta, Av. Angamos 601, Antofagasta, Chile

<sup>37</sup> MonitorMyPlanet, Toronto, Canada

<sup>38</sup> Tycho Tracker, USA

<sup>39</sup> Department of Physics, University of California, Santa Barbara, USA

<sup>40</sup> Astronomical Institute of the Romanian Academy, 5 Cuțitul de Argint, 040557 Bucharest, Romania

<sup>41</sup> Sugarloaf Mountain Observatory, South Deerfield, MA, USA

<sup>42</sup> Departamento de Matemática y Física Aplicadas, Facultad de Ingeniería, Universidad Católica de la Santísima Concepción, Alonso de Rivera 2850, Concepción, Chile

<sup>43</sup> Fesenkov Astrophysical Institute, Almaty, Kazakhstan

<sup>44</sup> University of Hawaii, USA

<sup>45</sup> Departamento de Física, Ingeniería de Sistemas y Teoría de la Señal, Universidad de Alicante, Carr. de San Vicente del Raspeig, s/n, E-03690 San Vicente del Raspeig, Alicante, Spain

<sup>46</sup> Institut de Ciències del Cosmos (ICCUB), Universitat de Barcelona (IEEC-UB), Carrer de Martí i Franquès, 1, E-08028, Barcelona, Spain

<sup>47</sup> Department of Physics and Astronomy FMPIT of Odesa I.I. Mechnykov National University, Pastera Street 42, 65082 Odesa, Ukraine

<sup>48</sup> Department of Physics and Methods of Teaching, Faculty of Physics and Technology, Vasyl Stefanyk Precarpathian National University, Shevchenko Street 57, 76000 Ivano-Frankivsk, Ukraine

Received 2023 September 21; revised 2023 October 27; accepted 2023 October 30; published 2024 February 7

## Abstract

On 2022 September 26, the Double Asteroid Redirection Test (DART) spacecraft impacted Dimorphos, the satellite of binary near-Earth asteroid (65803) Didymos. This demonstrated the efficacy of a kinetic impactor for planetary defense by changing the orbital period of Dimorphos by 33 minutes. Measuring the period change relied heavily on a coordinated campaign of lightcurve photometry designed to detect mutual events (occultations and eclipses) as a direct probe of the satellite’s orbital period. A total of 28 telescopes contributed 224 individual lightcurves during the impact apparition from 2022 July to 2023 February. We focus here on decomposable lightcurves, i.e., those from which mutual events could be extracted. We describe our process of lightcurve decomposition and use that to release the full data set for future analysis. We leverage these data to place constraints on the postimpact evolution of ejecta. The measured depths of mutual events relative to models showed that the ejecta became optically thin within the first  $\sim 1$  day after impact and then faded with a decay time of about 25 days. The bulk magnitude of the system showed that ejecta no longer contributed measurable brightness enhancement after about 20 days postimpact. This bulk photometric behavior was not well represented by an  $HG$  photometric model. An  $HG_1G_2$  model did fit the data well across a wide range of phase angles. Lastly, we note the presence of an ejecta tail through at least 2023 March. Its persistence implied ongoing escape of ejecta from the system many months after DART impact.

*Unified Astronomy Thesaurus concepts:* [Near-Earth objects \(1092\)](#); [Asteroids \(72\)](#); [Small Solar System bodies \(1469\)](#)

*Supporting material:* machine-readable table

## 1. Introduction

Binary systems are estimated to represent about 15% of the near-Earth asteroid population (Pravec et al. 2006). Discovered as a binary in 2003 November (Pravec et al. 2003), the near-Earth asteroid (65803) Didymos is an  $\sim 760$  m oblate spheroid with a  $\sim 150$  m satellite known as Dimorphos (Naidu et al. 2020; Daly et al. 2023). Based on extensive lightcurve (Pravec et al. 2022) and radar (Naidu et al. 2020) observations, the binary dynamics of this system have been well established (Naidu et al. 2022; Scheirich & Pravec 2022). Didymos has a rotation period =  $2.2600 \pm 0.0001$  hr, and Dimorphos had an orbit period =  $11.921481 \pm 0.000016$  hr (Naidu et al. 2022). This orbit period uncertainty of  $<60$  ms makes Didymos one of the best-characterized binary asteroids in the solar system. Such precision was achievable because Didymos is an eclipsing binary. Mutual events—occultations and eclipses—can be detected in time series photometry of Didymos and thus can serve as a chronometer for the orbital period of Dimorphos.

Given the state of knowledge of the Didymos system and favorable observing apparitions in the 2020s, this system was selected as the target for NASA’s Double Asteroid Redirection Test (DART) mission (Cheng et al. 2016; Rivkin et al. 2021). Following its launch from Vandenberg Space Force Base on 2021 November 24 and a relatively short 10 month cruise phase, the DART spacecraft intentionally impacted Dimorphos on 2022 September 26 (at JD 2459849.46834). This was the world’s first full-scale planetary defense experiment and was designed to change the orbital period of Dimorphos as a test of asteroid deflection via kinetic impactor. In terms of level 1 mission requirements (Rivkin et al. 2021), the impact by DART was to change the orbit period by at least 73 s, which would then be measured via ground-based observations to a

precision of 10% or 7.3 s (0.002 hr). DART impacted Dimorphos head-on (Daly et al. 2023) so that its orbital period decreased.

The DART spacecraft had a relatively simple payload that included a high-resolution imager called the Didymos Reconnaissance and Asteroid Camera for Optical navigation (DRACO; Fletcher et al. 2018) and a 6U CubeSat called the Light Italian CubeSat for Imaging of Asteroids (LICIACube; Dotto et al. 2021), built by the Italian Space Agency (ASI). LICIACube separated from the DART spacecraft 2 weeks before impact and provided flyby imagery of the impact ejecta plume from about 30 to 320 s after impact (Dotto & Zinzi 2023). Following these in situ operations, continued characterization of the system relied on remote telescopic observations.

An extensive campaign of ground- and space-based observations was coordinated to study the aftermath of the DART impact and meet the level 1 requirements of the mission. The primary component of this campaign involved lightcurve photometry and the measurement of mutual events (Section 2). Based on the analysis of lightcurves from prior apparitions (Pravec et al. 2022), the methodology for this campaign was well established. In short, high-quality photometry (rms residuals of generally  $<0.01$  mag) was needed to enable the decomposition of lightcurves (Section 4) into their constituent parts: the 2.26 hr rotation of Didymos, a possible rotational signature from Dimorphos, drops in flux due to mutual events, and, in the postimpact environment, the evolution of ejecta. These stringent data requirements had to be sustained across many facilities, many hours for each lightcurve, and the duration of the apparition. Observing circumstances such as apparent magnitude and declination, influenced campaign planning. For example, large-aperture facilities were primarily used at the beginning and end of the apparition when Didymos was faintest. Overall, this coordinated approach proved highly successful, yielding from just the first month of postimpact data a new orbital period for



Original content from this work may be used under the terms of the [Creative Commons Attribution 4.0 licence](#). Any further distribution of this work must maintain attribution to the author(s) and the title of the work, journal citation and DOI.

Dimorphos of  $11.372 \pm 0.017$  hr, corresponding to a change of  $-33$  minutes relative to the preimpact value (Thomas et al. 2023). In this work, we expand the scope of the lightcurve data set from that presented in Thomas et al. (2023) to now include a full 8 months of data across the 2022–2023 apparition.

For definitional purposes, we hereafter refer to a *lightcurve* as a time series of photometry collected by a single facility on a single night. A *lightcurve session* or *observing run* refers to the window in which a single lightcurve was obtained. We refer to the *primary lightcurve* as the rotational signature of Didymos. The term *secondary* refers to Dimorphos. Mutual events come in four flavors: *secondary eclipses* (Dimorphos passes into shadow), *secondary occultations* (Dimorphos moves behind Didymos), *primary eclipses* (the shadow of Dimorphos passes over Didymos), and *primary occultations* (Didymos is covered by Dimorphos).

In total, 28 observatories contributed data that were accepted as part of the DART lightcurve campaign (Section 3). This produced a massive data set of 224 lightcurves with hundreds of mutual events detected from 2022 July to 2023 February. The associated decompositions (Section 5) provided a basis for detailed modeling of the orbital and rotational dynamics in the Didymos system (Naidu et al. 2023; Scheirich et al. 2024). We note that these two modeling efforts represent independent assessments of the lightcurve data set. The lightcurves presented here are a superset of the data analyzed in Scheirich et al. (2024) because their data quality requirements were more stringent, resulting in 193 lightcurves accepted for their analysis. These two analyses were meant to be completely independent, so it is expected that different acceptance criteria were applied. However, the Naidu et al. (2023) and Scheirich et al. (2024) orbit solutions agree within formal uncertainties, a good indication that the less stringent approach here did not bias the results.

Our primary objective here is to provide an overview of the lightcurve campaign, associated data sets, and analysis; however, we also leverage these data to address the evolution of postimpact ejecta. The measured depths of mutual events served as a proxy for the optical depth and fading of ejecta (Section 6). The photometry of Didymos, averaged over lightcurve variations, allowed for characterizing the photometric phase curve and determining when ejecta no longer contributed significant flux to the system (Section 7). Lastly, ejecta in the form of an extended tail persisted through to the end of the apparition; we quantify the tail’s contribution to the total flux as a function of time (Section 8). Modeling of the dynamics of the Didymos system and refinements to the orbital period change of Dimorphos are presented elsewhere (e.g., Naidu et al. 2023; Scheirich et al. 2024). Discussion of our results and prospects for future work serve as a conclusion to this paper (Section 9).

## 2. DART Lightcurve Campaign

The Didymos system underwent a highly favorable apparition in 2022–2023 (Figure 1). This apparition was unusually long, with Didymos positioned at solar elongations greater than  $100^\circ$  for nearly 11 months, from 2022 May to 2023 April. During this time, the system was predicted to reach a peak brightness of  $V=14.5$  mag at the end of 2022 September, coincident with the DART impact. Didymos only gets this bright every few decades. The last time it was brighter than 15th magnitude was in 2003, when Dimorphos was discovered

(Pravec et al. 2003). It will not get this bright again until 2062 October. At these magnitudes, obtaining high-quality photometry is possible across a wide range of telescope apertures. We show in the following sections that telescope apertures down to 0.5 m in diameter were able to achieve strict data quality requirements and thus made significant contributions to the lightcurve campaign. Achieving the mission’s level 1 requirement of measuring the orbital period change of Dimorphos from ground-based facilities (Rivkin et al. 2021) was largely possible because of the system brightness in this apparition.

The viewing geometry of Didymos in the impact apparition was in some ways advantageous. For example, a wide range of solar phase angles, from a maximum of  $76^\circ$  to a minimum of  $6^\circ$ , enabled photometric (e.g., Section 7) and polarimetric (e.g., Bagnulo et al. 2023) phase curve analyses. However, the ranges of declination and Galactic latitude (Figure 1) posed interesting challenges. Given moderate negative declinations (around  $-35^\circ$ ) in the days after impact followed by a transition into northern declinations in late October, the observing campaign necessitated a global approach that leveraged telescopes in both the Northern and Southern Hemispheres. A Galactic plane crossing 24 days after impact (on 2022 October 20) was expected to degrade the quality of the photometry due to contamination by background sources for at least a week or two in late October. This turned out not to be a significant issue, as viable lightcurves were obtained throughout the Galactic plane crossing (Section 4). More problematic was the high background and low elongation from a full Moon on 2022 October 9. This led to a gap in viable lightcurves for about a week in the middle of the month. Fortunately, the postimpact brightening of Didymos by about 1.5 mag (Graykowski et al. 2023) allowed for short exposure times and thus helped to mitigate these issues of crowded fields and high background.

Taking these observational factors into account, the mission developed a 2022–2023 observing plan that spanned nine individual lunations, with the impact lunation split into pre- and post-DART impact windows (Table 1). The lunations represented windows outside of full Moon conditions when the highest-quality data were likely to be obtained. These covered the full apparition starting in 2022 July with preimpact lunations L1–L4 and then postimpact lunations that increased from L0 to L5, ending in 2023 February. Data were obtained after the L5 lunation in 2023 March, but insufficient temporal coverage and low signal-to-noise ratios (S/N) rendered these data unusable for our analysis here. Unsurprisingly, the number of viable lightcurves and associated decompositions (Table 1) tracked inversely with the apparent magnitude of Didymos. At the beginning (Pre-L1) and end (L5) of the apparition, when Didymos was faintest, telescopes with apertures  $>2$  m in diameter were required to collect data of sufficient quality. The primary goal of observations in the preimpact lunations was to confirm the dynamics of the system as determined by Naidu et al. (2022) and Scheirich & Pravec (2022). There was also interest in measuring the rotation period of Dimorphos in the preimpact data, but that signature was never clearly detected, perhaps due to its oblate shape (Daly et al. 2023).

For all lunations, the mission established strict data quality requirements to ensure successful lightcurve decompositions (Section 4). These requirements were largely based on experience gained from previous apparitions in 2003, 2015,

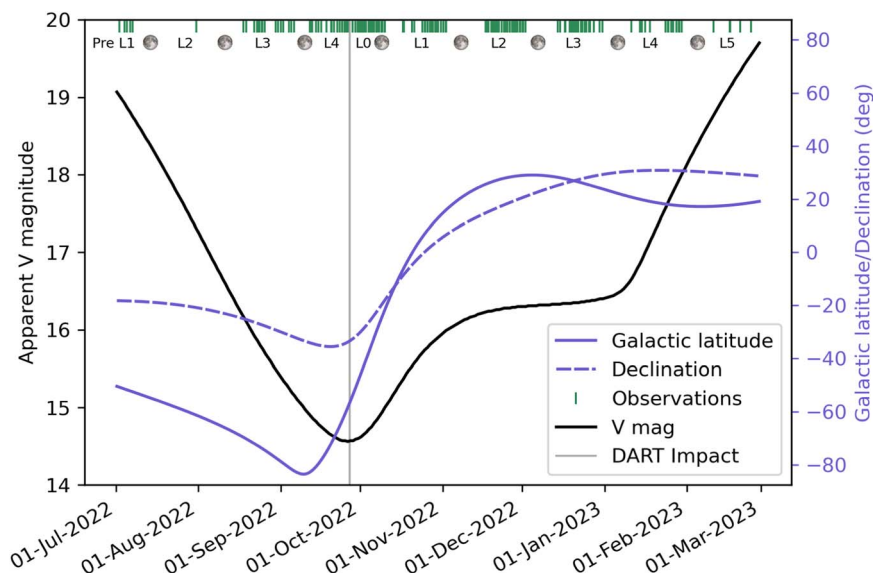


**Figure 1.** Observing circumstances for Didymos in the 2022–2023 apparition. The start dates of individual lightcurves (Table A1) are indicated across the top as green vertical bars. Labels for pre- and postimpact lunations are shown along with full Moon dates. The apparent magnitude, Galactic latitude, and declination of Didymos were calculated from Lowell Observatory’s astorb system (Moskovitz et al. 2022). Didymos reached a minimum magnitude of  $V = 14.5$  coincident with the DART impact on 2022 September 26 (vertical gray line). Gaps in lightcurve coverage were generally due to the full Moon; however, a Galactic plane crossing in mid-October also affected the number of viable lightcurves.

2017, 2019, 2020, and 2021 (e.g., Naidu et al. 2022; Pravec et al. 2022; Scheirich & Pravec 2022). Requirements provided to observers leading up to the apparition included photometric precision of at least  $0.01 \text{ mag exposure}^{-1}$  and a temporal cadence of no more than 180 s between exposures to ensure adequate sampling of mutual events. The choice of photometric filter was not prescribed because our primary photometric analysis was based on differential magnitudes, and we assumed that Didymos had no rotational color variability that would affect combining data from different filters. Observers were encouraged to employ whatever filter would yield the highest S/N with their instrument. Typically, lightcurves were accepted for analysis only if they spanned at least one full rotation of Didymos (2.26 hr), though exceptions were made for some short lightcurve segments when data from other facilities were taken close enough in time to enable a clean decomposition. These short segments were often useful in filling out specific rotational phases of Didymos that were not covered by adjacent lightcurves. Decompositions were performed on batches of data in which the morphology of the Didymos lightcurve was roughly constant. We discuss this process in greater detail in Section 4.

Though observations were planned in the days immediately after impact to monitor the evolution of the ejecta plume, the clearing of ejecta and its contribution to the measured photometry of the system was expected to confuse the detection of mutual events for many days or even weeks after impact (Fahnestock et al. 2022). Given the full Moon on October 9 and the Galactic plane crossing a little over a week later (Figure 1), it was unclear whether mutual event detections and thus a period change determination would be possible in the first month after impact. Thus, the lightcurve campaign had to be both comprehensive (e.g., facilities spanning a range of apertures and locations on Earth) and flexible (e.g., in telescope scheduling) to effectively respond to whatever was the outcome of the impact experiment.

To help observers prepare for postimpact observational challenges, such as low Galactic latitude and a bright Moon, a list of practice targets was provided. This list was intended to help test and refine the capabilities of instruments under challenging conditions and to help establish data analysis procedures that would enable rapid turnaround of reduced lightcurves. Test targets were selected from the catalog of known asteroids in the astorb database (Moskovitz et al. 2022) that had analogous observing conditions to Didymos in 2022 October. Specifically, we selected near-Earth objects with  $14.5 < V < 16.5$ , solar elongation  $>90^\circ$ , and nonsidereal rates of motion between  $1''.25$  and  $7''.5 \text{ minute}^{-1}$ . This list of test targets was posted online and dynamically updated on a daily basis to incorporate newly discovered objects and handle changes in observability. This list was additionally subdivided based on conditions related to lunar phase, lunar elongation, and Galactic latitude. Three windows of observing conditions were defined: (1) lunar phase  $>75\%$ , lunar elongation  $>60^\circ$ , and Galactic latitude  $>20^\circ$ ; (2)  $25\% < \text{lunar phase} < 75\%$ ,  $30^\circ < \text{lunar elongation} < 50^\circ$ , and Galactic latitude  $<10^\circ$ ; and (3) lunar phase  $<25\%$ , lunar elongation  $>45^\circ$ , and Galactic latitude  $<20^\circ$ . These three windows represented the conditions for Didymos from October 1 to 11, October 15 to 19, and October 20 to 27, respectively. For the year leading up to impact, any given night was likely to have  $\sim$ one to three test targets available that met these conditions.

The full extent of the 2022–2023 campaign involved contributions from many observers and facilities across the globe. Details of the 224 individual lightcurves presented in the remainder of this work are given in Appendix Table A1. For completeness, we include here data collected by the investigation team from 2022 July to 2023 February. Some of these observations (UT 2022 July 2–7, 2022 September 28–October 10) were previously reported in Thomas et al. (2023). We present only those data that met the quality requirements described above. Many dozens of additional data sets (about 25% of those submitted by the investigation team) were

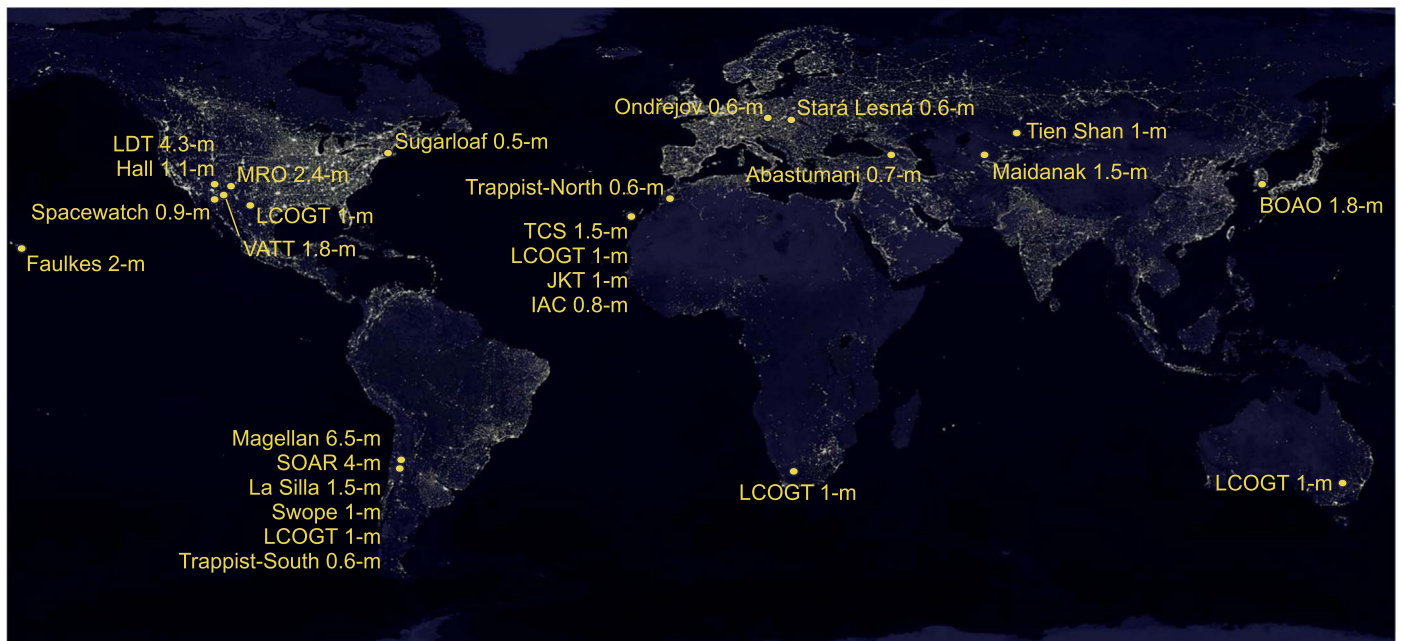


**Figure 2.** Global distribution of telescopes that contributed lightcurves to the 2022–2023 campaign. See text for details of facilities and instruments. Earth at night image credit: NASA/NOAA.

**Table 1**  
DART Campaign Lunations

Lunation	Data Range (JD)	Data Range (UTC)	Lightcurves	Decompositions
Pre-L1	2459762.6669 – 2459767.9728	2022-07-02T04:00 – 2022-07-07T11:20	5	1
Pre-L2	2459791.6504 – 2459791.9057	2022-07-31T03:36 – 2022-07-31T09:44	1	1
Pre-L3	2459809.5313 – 2459828.6771	2022-08-18T00:45 – 2022-09-06T04:15	16	4
Pre-L4	2459834.5636 – 2459848.8959	2022-09-12T01:31 – 2022-09-26T09:30	22	3
L0	2459850.6063 – 2459862.7933	2022-09-28T02:33 – 2022-10-10T07:02	54	13
L1	2459869.6181 – 2459886.0129	2022-10-17T02:50 – 2022-11-02T12:18	27	4
L2	2459900.7059 – 2459915.9442	2022-11-17T04:56 – 2022-12-02T10:39	48	7
L3	2459927.9180 – 2459944.8952	2022-12-14T10:01 – 2022-12-31T09:29	30	6
L4	2459955.5764 – 2459974.7416	2023-01-11T01:50 – 2023-01-30T05:47	16	2
L5	2459986.5711 – 2460000.8285	2023-02-11T01:42 – 2023-02-25T07:53	5	2

**Note.** The range of dates in which data were obtained are given for preimpact lunations L1–L4 and postimpact lunations L0–L5. The number of individual lightcurves and decompositions are given for each lunation.

unfortunately not accepted as viable for lightcurve analysis. However, some of these data sets have provided and will continue to provide valuable insights into other aspects of the postimpact Didymos environment (e.g., Kareta et al. 2023).

### 3. Telescope Facilities

A total of 28 telescopes contributed viable data to the lightcurve campaign (Figure 2, Table 2). These telescopes ranged in diameter from 0.5 up to 6.5 m and employed a wide variety of instruments. In addition, the photometric filters and tracking modes (sidereal versus nonsidereal) varied from one facility to the next. This approach to building the lightcurve data set was a natural consequence of the diversity and scope of the DART investigation team and may have helped to minimize systematic biases that could have affected outcomes if fewer facilities were involved. Careful control of systematics and data quality were essential to the success of the campaign and were the primary challenge to building the full data set. Though the general methodology of collecting images with

CCD cameras and measuring lightcurves is hardly novel, the DART campaign required that this be done at high precision (subpercent photometry) across a large number of facilities and be sustained for multiple hours within a night and across many months throughout the apparition.

To achieve these high standards, individual observers were encouraged to adopt whatever reduction methods worked best for their data. However, some aspects of the reductions were common to most data sets. In the postimpact window, aperture sizes significantly larger than the local seeing ( $5''$ – $7''$  radius for many of the data sets in October) were typically used to account for the extended brightness of the ejecta cloud. This was important to compensate for centroiding errors related to the complicated point-spread function of the postimpact system. It was found that the larger apertures generally caused higher noise levels in individual data points but much better point-to-point consistency across each lightcurve. In nearly all cases, circular aperture photometry was employed. Reductions involved testing a range of photometric aperture sizes to optimize both the S/N of individual measurements and the

**Table 2**  
Details of Facilities that Contributed to the 2022–2023 Lightcurve Campaign

Telescope	Instrument	Location	IAU Code(s)	No. of Lightcurves
6.5 m Magellan Baade	IMACS	Las Campanas, Chile	269	1
4.3 m LDT	LMI	Happy Jack, Arizona, USA	G37	8
4.1 m SOAR	Goodman	Cerro Pachón, Chile	I33	2
2.4 m MRO	MRO2k CCD	Magdalena Ridge, New Mexico, USA	H01	11
2.0 m FTN	MuSCAT3	Haleakala, Hawaii, USA	F65	1
1.8 m VATT	STA 4k CCD	Mount Graham, Arizona, USA	290	2
1.8 m BOAO	e2v 4k CCD	Bohunsan, South Korea	344	2
1.5 m Danish Telescope	DFOSC	La Silla, Chile	W74	42
1.5 m AZT-22 Telescope	SNUCAM	Maidanak Observatory, Uzbekistan	188	2
1.5 m TCS	MuSCAT2	Tenerife, Spain	954	4
1.1 m Hall Telescope	NASA42	Anderson Mesa, Arizona, USA	688	27
1 m LCOGT	Sinistro	McDonald Observatory, Texas, USA	V37, V39	5
1 m LCOGT	Sinistro	Siding Spring, Australia	Q63, G64	2
1 m LCOGT	Sinistro	Sutherland, South Africa	K91, K92, K93	9
1 m LCOGT	Sinistro	Cerro Tololo, Chile	W85, W86, W87	11
1 m LCOGT	Sinistro	Tenerife, Spain	Z31, Z24	10
1 m JKT	Andor 2k CCD	La Palma, Spain	950	2
1 m Swope Telescope	e2v 4k CCD	Las Campanas, Chile	304	19
1 m Tien-Shan Telescope	Apogee 3k CCD	Tien-Shan, Kazakhstan	N42	1
0.9 m Spacewatch	4-CCD mosaic	Kitt Peak, Arizona, USA	691	14
0.8 m IAC80	CAMELOT2	Observatorio del Teide, Spain	954	1
0.7 m AC-32 Telescope	FLI 2k CCD	Abastumani, Georgia	119	5
0.6 m Ondřejov Telescope	Moravian 2k CCD	Ondřejov, Czech Republic	557	4
0.6 m Sugarloaf Telescope	SBIG 2k CCD	Deerfield, Massachusetts, USA	...	4
0.6 m G2 Telescope	FLI 2k CCD	Stará Lesná Observatory, Slovakia	...	1
0.6 m TN	Andor iKon-L BEX2	Oukaïmeden Observatory, Morocco	Z53	8
0.6 m TN	FLI ProLine 3041-BB	La Silla, Chile	140	25
0.5 m T72 iTelescope	FLI 4k CCD	Deep Sky Chile Observatory, Chile	X07	1

**Note.** IAU assigned observatory codes are given when available. The number of individual lightcurves contributed by each facility is listed in the final column.

consistency of intranight measurements. In general, the magnitudes reported by each facility were converted to differential values by subtracting off the mean of each lightcurve outside of mutual events. Though error bars were reported for most lightcurves, these were not measured in a consistent way across all data sets and thus were largely ignored in our analysis.

Some telescopes elected to track at half of the nonsidereal rates of the asteroid. This was particularly true around the time of minimum geocentric distance, when the nonsidereal rates reached a maximum of  $\sim 8'' \text{ minute}^{-1}$ . Fortunately, the asteroid was also brightest at this time, and thus long exposures were not required. Generally, exposures times were kept below the level where significant elongation of the point-spread function occurred, eliminating the need for noncircular apertures. Noise characteristics for these data were dominated by the signal from the asteroid (and its morphologically complex ejecta cloud), as opposed to being background-limited. Thus, the use of circular apertures for these data, when the asteroid and stars may have been slightly trailed, did not introduce significant background noise into the measurements.

As a way to ensure that the period change measurement was adequately supported, the DART project contracted several facilities to carry out lightcurve observations. These included the 6.5 m Magellan Baade and 1 m Swope telescopes at Las Campanas Observatory in Chile, the 2.4 m Magdalena Ridge Observatory (MRO) in New Mexico, the 4.3 m Lowell Discovery Telescope (LDT) in Arizona, and the Las Cumbres Observatory Global Telescope (LCOGT) network of 1 m facilities. All other facilities that contributed to the lightcurve

campaign were not directly contracted by the project. These unsupported observatories contributed a majority of the lightcurves to the overall data set and serve as a testament to the global interest in the DART experiment.

In the following subsections, we summarize in order of aperture size the telescope, instrument, and reduction methods used by each facility. Details on individual lightcurves are in [Appendix Table A1](#). In addition, a large file is included with this manuscript as supporting data that contains all of the individual lightcurve measurements (38,532 in total) and the associated decomposed residuals that were used for mutual event analysis (Section 4). All original fits files from the contracted facilities will be made publicly available through NASA’s Planetary Data System Small Body Node.

### 3.1. 6.5 m Magellan-Baade

The Baade 6.5 m telescope is located at Las Campanas Observatory, in the Atacama Desert in the north of Chile, at an elevation of 2400 m. We employed the Inamori-Magellan Areal Camera and Spectrograph (IMACS) instrument (Dressler et al. 2011), which is equipped with two arrays of eight  $2k \times 4k$  e2v detectors, where each array provides a different pixel scale. Only the IMACS-F2 array with detector number 2 was used for this project, which has  $15 \mu\text{m}$  pixels that each image  $0.2''$  when unbinned. The asteroid was observed with a Sloan  $r$  filter and fixed pointings on the sky, letting the asteroid cross the detector’s field while changing to a new pointing when necessary.

The IMACS-F2 raw images were processed in the standard way, i.e., bias subtraction and flat-fielding. Astrometry was

performed with our own Python scripts built using the *astropy* package. Aperture photometry was measured on the asteroid and a selection of the brightest stars in every pointing to estimate the individual image zero-points and the differential photometry of the asteroid. The photometry was measured using our own Python scripts and the SEP Python library (Barbary 2018) source extraction tools. For the zero-points, the stars were matched against the Gaia DR3 catalog (Gaia Collaboration et al. 2021) when possible and against the PanSTARRS catalog when not.

### 3.2. 4.3 m Lowell Discovery Telescope (LDT)

The LDT is located in Happy Jack, Arizona, at an elevation of 2360 m. All LDT images were obtained with the Large Monolithic Imager (LMI), a  $6k \times 6k$  e2v CCD with  $15 \mu\text{m}$  pixels. LMI images a  $12'$  field of view at an unbinned pixel scale of  $0''.12 \text{ pixel}^{-1}$ . All images were obtained in  $3 \times 3$  binning mode with a broad VR filter that provided high throughput from about 500 to 700 nm. For all LDT observations, the telescope was tracked at sidereal rates, allowing the asteroid to pass through fixed star fields. Multiple pointings were used in a single night when the motion of the asteroid exceeded the instrument field of view. Individual exposure times ranged from 15 to 160 s across the apparition.

The reduction of LMI images followed standard flat-field and bias correction techniques. The photometry of Didymos was measured and calibrated using the Python-based Photometry Pipeline (PP; Mommert 2017) as described in Pravec et al. (2022). In summary, PP employed SExtractor (Bertin & Arnouts 1996) to extract sources from the fields, Scamp (Bertin 2006) to register the astrometry of those sources relative to the Gaia DR2 reference catalog (Gaia Collaboration et al. 2018), and then calibrated the photometry relative to the PanSTARRS Data Release 1 catalog (PS DR1; Flewelling et al. 2020). Only field stars with solar-like colors (i.e.,  $g-r$  and  $r-i$  colors within 0.2 mag of the Sun) were used for photometric calibration. Typically, more than 10 field stars were used to calibrate each image. A curve-of-growth analysis was performed each night to optimize the photometry aperture. This analysis aimed to optimize both the S/N of individual measurements and the consistency of intranight measurements to minimize point-to-point scatter. Aperture radii ranged from 3.5 to 7 pixels ( $1''.26$ – $2''.52$ ) across the apparition.

### 3.3. 4.1 m Southern Astrophysical Research (SOAR) Telescope

The SOAR telescope is located on Cerro Pachón in central Chile at an elevation of 2713 m. Images were obtained with the Goodman spectrograph and imager (Clemens et al. 2004), which employs an e2v 231-84 CCD with  $4k \times 4k$  pixels. In imaging mode, the CCD receives a  $7'.2$  circular field of view on a  $3k \times 3k$  portion of the chip. The unbinned pixel scale is  $0''.15 \text{ pixel}^{-1}$ . We operated the camera in  $2 \times 2$  binning mode with a VR filter that provided high throughput from approximately 500 to 700 nm. Individual image exposure times were 90 s.

The reduction and measuring of photometry from the SOAR data followed an identical procedure to that used for LDT. The PP referenced the Gaia DR2 (Gaia Collaboration et al. 2018) and PanSTARRS (Flewelling et al. 2020) catalogs for astrometric and photometric calibration. Aperture radii of 7

pixels ( $2''.1$ ) and 6 pixels ( $1''.8$ ) were used on the nights of UT 2022 July 4 and 2022 July 5, respectively.

### 3.4. 2.4 m Magdalena Ridge Observatory (MRO)

The MRO fast-tracking 2.4 m telescope is located at an elevation of 3250 m in the Magdalena Mountains near Socorro, New Mexico. All MRO images were acquired with MRO2K, which is an Andor iKon-L 936 camera operating at 188K, utilizing a  $2048 \times 2048$  back-illuminated e2v CCD with  $13.5 \mu\text{m}$  pixels. The unbinned pixel scale is  $0''.13 \text{ pixel}^{-1}$  yielding a  $4'.5$  field of view. All lightcurve data were acquired in  $4 \times 4$  binning mode using either the Bessell R or broadband VR filter while tracking on Didymos to maximize its signal. Observations early in the apparition required separate images of comparison star fields due to Didymos's rapid nonsidereal motion. For this reason, this time period also necessitated having photometric sky conditions. Exposure times ranged from 15 to 150 s throughout the apparition.

MRO images were reduced according to standard dark, bias, and flat-field correction techniques. The photometry of Didymos was measured using the IRAF Aperture Photometry (APHOT) package (Tody 1986). The instrumental magnitude of Didymos was measured in each field using apertures that ranged from 4 to 10 pixels ( $2''.1$ – $5''.2$ ) depending on seeing conditions. In addition, an ensemble of typically five to eight stars in each comparison field was also measured in either the same image or a separate comparison star image. An initial analysis was performed on the comparison stars to assess their robustness. A temporally interpolated average magnitude of the comparison stars was then subtracted from each Didymos instrumental magnitude, resulting in a differential magnitude. The resulting lightcurve magnitudes were then reported as “relative” with an arbitrary zero-point.

### 3.5. 2.0 m Faulkes North

Faulkes Telescope North (FTN) is located on Haleakala, Maui, in Hawaii. FTN images were collected with MuSCAT3 (Narita et al. 2020), a four-channel simultaneous imager with  $g$ ,  $r$ ,  $i$ , and  $z$  channels. The four independent channels employ  $2k \times 2k$  Princeton Instruments CCDs from the Pixis and Sophia model lines. Each CCD images a  $9'.1$  field of view at a scale of  $0''.27 \text{ pixel}^{-1}$ . Individual exposure times were 30 s for all channels.

Reduction of the MuSCAT3 images employed the Astro-ImageJ (AIJ; Collins et al. 2017) package. Within AIJ, the multiple-aperture differential photometry tool was used to settle on an optimal aperture radius of 12 pixels and a background annulus with an inner radius of 15 and an outer radius of 20 pixels. The measured fluxes from each of the four simultaneous *griz* exposures were combined into a single arbitrary magnitude and then calibrated against the Gaia DR3 catalog (Gaia Collaboration et al. 2021). Four field stars per frame with roughly solar-like colors were used for this calibration.

### 3.6. 1.8 m Vatican Advanced Technology Telescope (VATT)

The VATT is located at Mount Graham, Arizona, and is an aplanatic Gregorian 1.8 m f/9 telescope with a 0.38 m f/0.9 secondary mirror. The VATT4K CCD camera was used for all VATT observations and consists of a STA0500A  $4096 \times 4096$  pixel back-illuminated detector with  $15 \times 15 \mu\text{m}$  pixels. VATT4K images have a  $12'.5$  field of view and were obtained



in a  $2 \times 2$  binning mode yielding a binned pixel scale of  $0''.38 \text{ pixel}^{-1}$ .

For VATT data, the telescope was tracked at sidereal rates with multiple pointings in a single night to keep the asteroid within the field of view. Individual exposures of 30 and 60 s in duration were taken through a Harris *V*-band filter. The reduction of VATT4K images followed standard flat-field and bias correction techniques. The observations were measured using the Tycho Tracker software (Parrott 2020) with photometry calibrated relative to the ATLAS stellar catalog (Tonry et al. 2018). Photometric calibration was derived from field stars with solar-like colors. A circular photometric aperture with a radius of 11 pixels ( $4''.1$ ) was used in conjunction with a sky background annulus with an inner radius of 23 pixels ( $8''.5$ ) and an outer radius of 33 pixels ( $12''.2$ ).

### 3.7. 1.8 m Bohyunsan Optical Astronomy Observatory (BOAO)

BOAO is located in Yeongcheon, Korea, at an altitude of 1143 m. Observations were conducted using the 1.8 m telescope at BOAO with an e2v 4k CCD and a Cousins *R* filter. All images were taken in  $2 \times 2$  binning mode with an effective pixel scale of  $0''.43 \text{ pixel}^{-1}$ , resulting in a field of view of  $14'.7 \times 14'.7$ . Individual exposure times were set to 100 s.

The images from BOAO were reduced using the IRAF software package. We performed calibration procedures, including bias, dark, and flat-field corrections, following standard protocols. To calculate the World Coordinate System (WCS) solution, we utilized the SCAMP package (Bertin 2006) and matched fields to the Gaia DR2 catalog (Gaia Collaboration et al. 2018). Aperture photometry was conducted on these images using the IRAF/APPHOT package. The aperture radius was set to 10 pixels ( $\sim 4''.5$ ) to minimize point-to-point scatter. The photometric calibrations were performed following the method of Gilliland & Brown (1988), namely, using ensemble normalization employing standard magnitudes obtained from the PS DR1 (Flewelling et al. 2020). For consistency, we converted the PS DR1 magnitudes to the Johnson–Cousins system using empirical transformation equations (Tonry et al. 2012).

### 3.8. 1.54 m Danish Telescope

The 1.54 m Danish Telescope is located at La Silla Observatory, Chile, at an elevation of 2366 m. It is operated jointly by the Niels Bohr Institute, University of Copenhagen, Denmark, and the Astronomical Institute of the Academy of Sciences of the Czech Republic. All images in the DART campaign were obtained by the Danish Faint Object Spectrograph and Camera (DFOSC) with an e2v CCD 231-41 sensor and standard Johnson–Cousins *V* and *R* photometric filters (Bessell 1990). The CCD sensor has  $2048 \times 2048$  square pixels ( $13.5 \mu\text{m}$  size), and we used it in  $1 \times 1$  binning mode to produce a scale of  $0''.396 \text{ pixel}^{-1}$  and a  $13.5 \times 13.5 \text{ arcmin}^2$  field of view. For the observations taken in September and the first half of 2022 October, the telescope was tracked at sidereal rates, allowing the asteroid to pass through fixed star fields. For the observations taken from 2022 October 29 to 2023 January 29, the telescope was tracked at half the apparent rate of the asteroid, providing star and asteroid images of the same profile in one frame that facilitated obtaining robust photometric reduction. Multiple pointings were used in a single night for the

observations taken in September and the first half of October, when the motion of the asteroid in a night exceeded the instrumental field of view. We used a single set of local reference stars for each night of observations from late 2022 October through late 2023 January. Individual exposure times ranged from 6 to 150 s across the apparition.

The reduction of the images followed standard flat-field and bias-frame correction techniques. The photometry of Didymos was measured and calibrated using *Aphot*, a synthetic aperture photometry software developed by M. Velen and P. Pravec at Ondřejov Observatory. It reduces asteroid images with respect to a set of field stars, and the reference stars are then calibrated in the Johnson–Cousins photometric system using Landolt (1992) standard stars on a night with photometric sky conditions. This resulted in *R*-magnitude errors of about 0.01 mag. Typically, eight local reference field stars, which were checked for stability (nonvariable, not of extreme colors), were used on each night or for each pointing on nights before mid-October. Aperture radii from 6 to 10 pixels ( $2''.4$ – $4''.0$ ) were found optimal on the individual nights.

### 3.9. 1.5 m AZT-22 telescope at Maidanak Observatory

The 1.5 m AZT-22 telescope is located in the western part of Maidanak Mountain in the south of Uzbekistan at an elevation of 2593 m. The Didymos observations were carried out with the Seoul National University  $4k \times 4k$  CCD Camera (SNU-CAM), which has  $4096 \times 4096$  square  $15 \mu\text{m}$  pixels with a CCD chip manufactured by Fairchild Instruments (Im et al. 2010). All images were obtained with an unbinned pixel scale of  $0''.27 \text{ pixel}^{-1}$  and a field of view  $18'.1 \times 18'.1$  through the *R* filter. The telescope was tracked at sidereal rates, and the exposure times were set to 60 s.

The primary reduction of images was performed in a standard way with master bias and master flats, the latter was constructed from twilight flats obtained on nearby nights under photometric conditions. Aperture photometry was performed using MPO Canopus.<sup>49</sup> The ATLAS catalog (Tonry et al. 2018) was used to obtain calibrated *R* magnitudes for the asteroid based on comparison stars with colors close to the Sun. Five solar-type stars were used to calibrate the frames. The diameter of the aperture used for the comparison stars was 11 pixels, or about  $3''$ . The images of the asteroid were slightly trailed over the 60 s exposures, so asteroid measurements were made with an elliptical aperture of  $11 \times 13$  pixels. These aperture dimensions were chosen to roughly approximate isophotes for the stars and asteroid.

### 3.10. 1.5 m Telescopio Carlos Sánchez (TCS)

The TCS belongs to the Instituto de Astrofísica de Canarias and is located at Teide Observatory (latitude  $28^\circ 18' 01''.8 \text{ N}$ ; longitude  $+16^\circ 30' 39''.2 \text{ W}$ ; altitude 2387 m). Typical seeing for this location is in the range of  $1''.0$ – $1''.5$ . The observations were performed with the MuSCAT2 instrument (Narita et al. 2019), which is mounted on the Cassegrain focus of the telescope. A system of lenses reduces the focal length of the system to a ratio of  $f/4.4$ .

This instrument allows simultaneous photometric observations in four visible broadband filters, namely, *g* (400–550), *r* (550–700), *i* (700–820), and *z<sub>s</sub>* (820–920) nm. At the end of

<sup>49</sup> <https://minplanobs.org/BdwPub/php/displayhome.php>

each of the four channels, there are independently controllable CCD cameras ( $1024 \times 1024$  pixels). They have a pixel size of  $\sim 0.44$  arcsec pixel $^{-1}$  and a field of view of  $7.4 \times 7.4$  arcmin $^2$ . The telescope was tracked at sidereal rates with the asteroid crossing the entire field of view. Because of the small field of view, multiple pointings were needed during the same observing session. The single image exposure times were 15 s for the first three sessions (UT 2022 September 30, 2022 October 7, and 2022 October 16) and 30 s for the last (UT 2022 November 16).

The preprocessing of the images included bias and flat-field corrections. The remaining background patterns were removed using the GNU Astro package (Akhlaghi & Ichikawa 2015; Akhlaghi 2019). The lightcurves were first measured with PP (Mommert 2017). For astrometric registration, we used the Gaia catalog (Gaia Collaboration et al. 2018). We discarded all images for which the astrometric registration failed (due to bad tracking or variable sky conditions). The PanSTARRS catalog (Flewelling et al. 2020) was used for photometric calibration. PP was run with a fixed aperture of  $4''.4$  (10 pixels).

A second data reduction was performed using IRAF (Tody 1986). In order to improve the S/N, we combined the images taken simultaneously by the four channels into a single one. Then, we performed differential photometry using the APPHOT package from IRAF. The magnitudes were computed using an aperture of  $4''.4$ , and nine comparison stars from the same field of view were used to compute the differential photometry. To further improve the S/N, we binned every four exposures into a single point. We then spliced lightcurve segments from different pointings into a single lightcurve. The offsets between the lightcurve segments were computed using the calibrated photometry derived with PP on the observations made with the  $g$  filter.

### 3.11. 1.1 m Hall

The 1.1 m Hall Telescope is located on Anderson Mesa, 9 air miles southeast of Flagstaff, Arizona, at an elevation of 2203 m. All images were taken with the NASA42 camera, a custom-built CCD camera with a  $4K \times 4K$  array of  $15 \mu\text{m}$  pixels. The image scale after applying  $3 \times 3$  binning was  $1.09$  arcsec pixel $^{-1}$ , with a field of view of  $24'$ . Images were taken through a broadband  $VR$  filter. In the first month after the DART impact, the Didymos system was moving at a rate of over  $6''$  minute $^{-1}$ . Therefore, tracking was done at half of the ephemeris rate of the asteroid, and three pointings were typically made during the night. Exposure times ranged from 90 to 180 s.

Data reduction began with image calibration with MaxIm DL,<sup>50</sup> using sets of 15 bias and flat frames that were typically collected at the beginning of each night. Groups of images at each pointing were astrometrically solved, registered, and aligned in MaxIm DL. Photometry was performed with MPO Canopus. Typically, five comparison stars with solar color ( $B - V$  color between 0.5 and 0.9) were used. Comparison star magnitudes were obtained from the ATLAS catalog (Tonry et al. 2018), which is incorporated directly into MPO Canopus. Star subtraction and outright rejection of frames were necessary in cases where the asteroid passed through dense star fields. The photometric aperture ranged from 7 pixels ( $7''.6$ ) to 13 pixels ( $14''.2$ ).

### 3.12. 1 m Las Cumbres Observatory Global Telescope Network (LCOGT)

LCOGT is a global network of 25 telescopes in three size classes at seven sites around the world (Brown et al. 2013). For the DART lightcurve observations, the 1.0 m telescope network was used, and observations were requested using the NEOexchange Target and Observation Manager (Lister et al. 2021) system. Data were obtained from LCOGT sites located at

1. Cerro Tololo Observatory, District IV, Chile (three 1.0 m telescopes; MPC site codes W85, W86, W87);
2. South African Astronomical Observatory, Sutherland, South Africa (three 1.0 m telescopes; MPC site codes K91, K92, K93);
3. McDonald Observatory, Fort Davis, Texas (two 1.0 m telescopes; MPC site codes V37, V39); and
4. Teide Observatory, Canary Islands, Spain (two 1.0 m telescopes; MPC site codes Z31, Z24).

All of the LCOGT 1.0 m images were obtained with the Sinistro instruments, each containing a  $4k \times 4k$  Fairchild CCD with  $15 \mu\text{m}$  pixels. The Sinistro imagers provide a  $26'.5 \times 26'.5$  field of view with an unbinned pixel scale of  $0''.389$  pixel $^{-1}$ . All images were obtained in  $1 \times 1$  binning mode with a PanSTARRS- $w$  filter (equivalent to SDSS  $g' + r' + i'$ ), which provided high throughput between 400 and 850 nm. The telescopes were tracking at half Didymos's on-sky ephemeris rate throughout the observations. Individual exposures times ranged from 27.5 to 150 s.

The reduction of the Sinistro images followed a two-step process. Initial reduction to basic calibrated data products involving bias and dark subtraction, flat-fielding, and astrometric fitting were performed automatically within minutes of readout of the frame by the LCOGT BANZAI pipeline (McCully et al. 2018). The basic calibrated data were then automatically retrieved from the LCOGT Science Archive and pipeline processed through the PP (Mommert 2017) and NEOexchange (NEOx; Lister et al. 2021) pipelines.

Both pipelines used SExtractor (Bertin & Arnouts 1996) to extract sources from the image and SCAMP (Bertin 2006) to perform the astrometric registration to the Gaia DR2 catalog (Gaia Collaboration et al. 2018) and then calibrated against PS DR1 (Flewelling et al. 2020) or the Gaia DR2 catalog, depending on the decl. of Didymos at the time of the observations. This zero-point calibration within the NEOx pipeline was performed using the *calviacat* (Kelley & Lister 2022) package. A preliminary reduction was generally done with the PP to perform a curve-of-growth analysis and an optimal aperture radius for the main NEOx reductions and to act as a cross-check on the reductions. Due to the low Galactic latitude of Didymos in the early 2022 October–November data and the variable and differential reddening of the field stars, we did not use the features of either PP or *calviacat* to restrict the field stars to having solar-like colors. Given the crowded fields, persistence of ejecta, fading of the target, and analysis focused on differential magnitudes, the choice of nonsolar-type stars for field calibration had no discernible influence on the quality of the photometry calibration.

### 3.13. 1 m Jacobus Kapteyn Telescope (JKT)

The JKT is equipped with an Andor 2k CCD camera and situated at the Roque de los Muchachos Observatory on La

<sup>50</sup> <https://diffractionlimited.com/product/maxim-dl/>

Palma. The telescope's field of view is  $11'.6 \times 11'.6$ , and the image scale is  $0''.34 \text{ pixel}^{-1}$ . The observations were obtained using the Johnson *R* filter, and we utilized sidereal tracking. Exposure times of 100 s were used.

Data from the JKT were processed using standard reduction procedures and aperture photometry, with the commercial software MPO Canopus following established procedures (e.g., Oszkiewicz et al. 2020, 2021, 2023). We selected five comparison stars in each field with significantly higher S/Ns than the target, ensuring they had roughly solar colors (approximately  $0.5 < B - V < 0.95$  or  $0.35 < g - r < 0.85$ ). An aperture 21 pixels in diameter was employed. For calibration, we used PS DR1 (Flewelling et al. 2020).

### 3.14. 1 m Swope

The Swope 1.0 m telescope is located at Las Campanas Observatory, in the Atacama Desert in the north of Chile, at an elevation of 2400 m. The Swope telescope is equipped with a  $4k \times 4k$  e2v detector with  $15 \mu\text{m}$  pixels covering a  $30' \times 30'$  area with  $0''.435$  pixels. The Swope data set encompassed a total of 8733 Sloan *r* images taken across 19 nights. In 5 of 15 nights, a single pointing was used to follow Didymos, while for the other nights, two pointings were necessary. For each pointing, the brightest 50 stars in the field were selected as standards to achieve photometric calibration of the individual images and estimate the differential photometry of the asteroid.

Swope images are read out by four amplifiers, producing four quadrant files for each exposure. Each of these quadrants was processed separately with standard techniques, namely, bias subtraction, linearity correction, and flat-fielding. After normalization by the individual gains, the full image was rebuilt as a single fits file. The astrometric solution was achieved with an iterative process, starting with a preliminary solution created using the WCS routine within the *astropy* package, and then improved by matching star positions against their Gaia coordinates. Instrumental aperture photometry was performed using the Python package SEP (Barbary 2018) on every image for the asteroid's and the brightest star's positions across a set of apertures from 3 to 20 pixels in radius. To estimate the photometric zero-points on individual images, we used several Python packages. *astroquery* was used to query the VizieR and Horizon databases to identify Gaia sources within  $2''$  of our set of bright field stars and obtain the coordinates of the asteroid for the given time stamp in each image. The *gaiaxy*<sup>51</sup> Python package was used to request and download synthetic photometry of Gaia stars (Gaia Collaboration et al. 2021) in the Sloan *r* band when available. We found more than 30 Gaia stars with available synthetic photometry in most pointings, and in only two cases did we retrieve fewer than 10 stars. This allowed us to determine robust statistics for the zero-points. For each image, we estimated a median, rejected outliers, and measured the standard deviation to provide an error on the zero-point, which was typically around  $0.01\text{--}0.02 \text{ mag frame}^{-1}$ . Final photometry of the Didymos–Dimorphos system was estimated by adding the zero-points to its instrumental magnitude for each image.

### 3.15. 1 m Zeiss Telescope at Tien-Shan Observatory

The 1 m Zeiss telescope at Tien-Shan Observatory is located at 2800 m altitude in the Almaty region of Kazakhstan. The

observations were carried out with the front-illuminated CCD camera PL09000 (made by Finger Lakes Instruments) with a sensor of  $3056 \times 3056$  pixels and a pixel size of  $12 \mu\text{m}$ . The images covered a  $19'.1 \times 19'.1$  field of view. The asteroid was observed with a Johnson–Cousins *R* filter. The observations were carried out with the telescope tracking at sidereal rates and the camera in  $2 \times 2$  binning mode (producing an image scale =  $0''.75 \text{ pixel}^{-1}$ ). At the end of December, the asteroid was moving across the sky at an angular rate of  $1''.2 \text{ minute}^{-1}$  and thus was trailed by about 2.4 pixels during the 90 s exposures.

Reduction of the images included removal of an average dark frame and normalization with a median dome flat field. Didymos's brightness was measured with the AstPhot software (Mottola et al. 1995). The size of the aperture was chosen to maximize the S/N based on measurements of several bright stars. An aperture radius of 6 pixels ( $4''.5$ ) was determined to be optimal. An elliptical aperture of  $6 \times 7$  pixels was used for the slightly elongated asteroid. As with the AZT-22 data, these apertures were chosen to roughly approximate isophotes for the stars and asteroid. The *R* magnitudes of comparison stars were taken from the ATLAS catalog (Tonry et al. 2018) and used to calibrate the asteroid using the MPO Canopus software package.

### 3.16. 0.9 m Spacewatch

SPACEWATCH<sup>®</sup> operates Steward Observatory's 0.9 m telescope on Kitt Peak, in Arizona, at an elevation of 2080 m. Images were obtained with the Spacewatch mosaic camera, a mosaic of four e2v  $4k \times 2k$  CCDs with  $13.5 \mu\text{m}$  pixels. It has an effective field of view of  $2.9 \text{ deg}^2$  at an unbinned pixel scale of  $1'' \text{ pixel}^{-1}$ . The images were obtained unbinned with a broadband Schott OG-515 filter, which has a long-pass transmission profile with a cut-on wavelength at 515 nm. Individual exposures ranged from 16 to 104 s across the apparition.

The reduction followed standard bias, flat-field, and fringe correction techniques. The photometry of the Didymos system was measured and calibrated using the PP (Mommert 2017) and MPO Canopus following the same procedures as applied to the LDT and Hall telescopes, respectively.

### 3.17. 0.8 m at the Instituto de Astrofísica de Canarias (IAC80)

The 0.8 m at the Instituto de Astrofísica de Canarias (IAC80) telescope, equipped with the CAMELOT2 instrument, is located at the Observatorio del Teide on Tenerife. CAMELOT2 features a  $4k \times 4k$  back-illuminated CCD. The on-sky pixel scale is  $0''.322 \text{ pixel}^{-1}$ , providing a theoretical field of view of  $22 \times 22 \text{ arcminutes}^2$ . However, due to vignetting caused by the filters, the useful squared field of view is  $11.8 \times 11.8 \text{ arcmin}^2$ . The data were obtained using the Johnson *R* filter, and sidereal tracking was employed. An exposure time of 135 s and aperture diameter of 19 pixels were used.

Data reduction and measurement of photometry for the IAC80 data followed the same procedures as used for data from the JKT (Section 3.13).

### 3.18. 0.7 m AC-32 Telescope of the Abastumani Astrophysical Observatory

The 0.7 m AC-32 telescope is a Maksutov meniscus telescope at the Abastumani Observatory, which is located on Konobili Mountain in the Samtskhe-Javakheti region of Georgia at an altitude of 1650 m. AC-32 is equipped with a back-illuminated  $2k \times 2k$  CCD camera PL4240 (made by Finger Lakes

<sup>51</sup> <https://gaia-dpci.github.io/GaiaXPY-website/>

Instruments) with  $13.5\ \mu\text{m}$  pixels. The camera is installed at the prime focus. AC-32 images a  $44'4$  field of view with an unbinned pixel scale of  $1''30$ . We employed a Johnson–Cousins  $R$  filter. All AC-32 observations were taken at sidereal rates. The exposures ranged from 120 to 180 s, depending on the observing circumstances.

The reduction of AC-32 images was performed using standard dark and flat-field corrections. The average flat field was calculated as a median of more than seven twilight sky flat images. Aperture photometry was used to measure brightness by means of the AstPhot software package (Mottola et al. 1995). An optimal aperture for field stars of 4–5 pixels ( $5''2$ – $6''5$ ) was used. An elliptical aperture for the asteroid was extended in the direction of its motion by 1–2 pixels. Again, these aperture dimensions were chosen to roughly approximate isophotes for the stars and asteroid. Relative photometry for the asteroid was performed by subtracting the magnitudes of nearby comparison stars. The comparison stars were chosen with colors close to the Sun. Uncertainties on the instrumental magnitudes of the comparison stars were usually around 0.002–0.005 mag. The comparison stars were calibrated to the Johnson–Cousins  $R$  band based on reference magnitudes from the ATLAS catalog (Tonry et al. 2018).

### 3.19. 0.65 m Ondřejov Telescope

The 0.65 m telescope is located at Ondřejov Observatory, Czech Republic, at an elevation of 528 m. It is operated jointly by the Astronomical Institute of the Academy of Sciences of the Czech Republic and the Astronomical Institute of the Charles University Prague, Czech Republic. All images in the DART campaign were obtained with a Moravian Instruments G2-3200 Mk. II CCD camera that uses a Kodak KAF-3200ME sensor and a standard Cousins  $R$  photometric filter (Bessell 1990) mounted in the prime focus with a Paracorr coma corrector. The CCD sensor has  $2184 \times 1472$  square pixels ( $6.8\ \mu\text{m}$  size) with microlenses, and we used it in  $2 \times 2$  binning mode that provided a scale of  $1''05\ \text{pixel}^{-1}$  and a  $19 \times 13\ \text{arcmin}^2$  field of view. For all observations presented here, the telescope was tracked at the half-apparent rate of the asteroid, providing star and asteroid images of the same profile in one frame. The asteroid moved slow enough during the observations so that we could use a single set of local reference stars for the observations taken on one night. Individual exposure times ranged from 90 to 180 s across the apparition.

The reduction of images followed standard flat-field and dark-frame correction techniques. The photometry was measured and calibrated in a manner identical to that employed for the 1.54 m Danish telescope. Aperture radii of 4 or 5 pixels ( $4''2$  or  $5''25$ ) were found optimal for data from the 0.65 m Ondřejov telescope.

### 3.20. 0.64 m at Sugarloaf Mountain Observatory

Sugarloaf Mountain Observatory is located in South Deerfield, Massachusetts, USA, at an elevation of 65 m. The telescope is a 0.64 m reflector. The imager is an SBIG Aluma 3200 CCD using the KAF-3200 chip. This chip contains an array of  $2184 \times 1472$  pixels unbinned. All images were taken using  $2 \times 2$  binning. The telescope has a field of view of  $23'2 \times 15'6$  and a working image scale of  $1''27\ \text{pixel}^{-1}$ . No filters were used to acquire images, and exposure times ranged from 70 to 100 s. Tracking was at the sidereal rate.

All images were processed using dark, bias, and flat-field corrections. Image reduction was accomplished using MPO Canopus software. Calculated magnitudes were based on an internal scale using several comparison stars that were selected to be similar to the solar color. The magnitudes of the comparisons were those in the  $R$  band in the Carlsberg Meridian Catalog (CMC15; Niels Bohr Institute et al. 2014). Measurement apertures were either 11 or 13 pixels in diameter ( $14''0$  or  $16''5$ ) depending on seeing.

### 3.21. 0.6 m G2 at Stará Lesná Observatory

The 0.60 m  $f/12.5$  Cassegrain telescope is situated near Stará Lesná village in Slovakia. It belongs to the Astronomical Institute and is located in the G2 pavilion. For imaging, it uses an FLI CCD camera with  $15\ \mu\text{m}$  pixels (unbinned). For observing Didymos, we used  $2 \times 2$  binning to produce an effective image resolution of  $0''85 \times 0''85$  and a field of view of  $14'5 \times 14'5$ . We used a Johnson–Cousins  $R$  filter. The telescope was set to track at sidereal rates so that the asteroid was moving through the field. The exposure time was set to 170 s. Light frames were reduced with dark frames and flat fields in a standard manner. For the photometric measurements, we used MaximDL6 with an aperture size of 11 pixels.

### 3.22. 0.6 m TRAPPIST-North and South

TRAPPIST-South (TS) is located at the ESO La Silla Observatory in Chile (Jehin et al. 2011). TRAPPIST-North (TN) is located at the Oukaïmeden Observatory in Morocco. Both TS and TN are robotic 0.6 m Ritchey–Chrétien telescopes operating at  $f/8$ . TS is equipped with an FLI ProLine 3041-BB CCD camera with a  $22'$  field of view and unbinned pixel scale of  $0''64\ \text{pixel}^{-1}$ . TN is equipped with an Andor iKon-L BEX2 DD camera providing a  $20'$  field of view and unbinned pixel scale of  $0''60\ \text{pixel}^{-1}$ . No binning was used for observations from September to the end of 2022 November, after which  $2 \times 2$  binning mode was used. The Exo filters were used, which are broad blue-blocking filters with a transmission from  $0.5\ \mu\text{m}$  to the NIR. Exposure times ranged from 45 to 120 s.

The raw images were processed using standard bias, dark, and flat-field frames. The photometry was measured using the PP (Mommert 2017) and calibrated to the  $R_c$  Johnson–Cousins band using the PS DR1. Typically, more than 50 field stars with solar-like colors were used in each image. The photometric apertures had fixed radii of 12 pixels for the unbinned observations and 6 pixels for the  $2 \times 2$  binning mode.

### 3.23. 0.5 m T72 at Deep Sky Chile Observatory

The T72 telescope of iTelescope is located in Rio Hurtado Valley, Chile, at an elevation of 1710 m. All T72 images were obtained with the KAF-16200 sensor, a  $4500 \times 3600$  CCD with  $6\ \mu\text{m}$  square pixels. KAF-16200 images a  $26'93 \times 21'53$  field of view at an unbinned scale of  $0''359\ \text{pixel}^{-1}$ . All images were obtained in  $2 \times 2$  binning mode with a Johnson–Cousins  $R$  filter. For all T72 data presented here, the telescope was tracked at sidereal rates, allowing the asteroid to pass through fixed star fields. Individual exposure times were 60 s.

The reduction of KAF-16200 images followed standard flat-field and bias correction techniques. The images were calibrated by the iTelescope pipeline. However, the alignment of the images, as well as plate solving and photometry, was performed using the software Tycho Tracker. Typically four to

seven field stars were used to calibrate each image. Aperture radii ranged from 4 to 8 pixels.

#### 4. Lightcurve Analysis

The primary objective of the lightcurve campaign was to detect mutual events that could then be used to determine the orbital period of Dimorphos. This required grouping lightcurves into decomposable sets of 1–14 individual lightcurves, where each set was collected over the span of 1 up to a few days. As a rough general rule, coverage across at least two rotations of Didymos ( $\sim 4.5$  hr) outside of mutual events was needed for a successful decomposition. Decomposition sets were defined based on the morphology of the primary lightcurve. Namely, individual lightcurves were added to a decomposition set as long as the morphology of the primary lightcurve remained constant within the S/N of the data. A new decomposition set was defined when changes to the primary lightcurve were detected. A total of 43 decompositions were performed with 224 individual lightcurves (Table 3). Individual decompositions were given unique IDs indicating the lunation in which the data were obtained followed by an integer indicating the  $n$ th decomposition within the lunation. For example, the third set of decomposed lightcurves in the postimpact L0 lunation was assigned an ID of L0.3. These IDs facilitate mapping of information across Tables 1, 3, and A1 and the supporting data file that contains all of the lightcurve measurements.

Observers on the investigation team submitted lightcurves for decomposition as simple ascii files, typically containing JD, magnitude, and magnitude error. Our methodology for decomposing these lightcurves into their constituent parts can be summarized with the following steps, which are then described in more detail in the remainder of this section.

1. The observed JD values were light-time corrected to be in the reference frame of the asteroid.
2. For each individual lightcurve, magnitudes were differentially corrected for small changes in geometry (phase angle, geocentric range, heliocentric range) within the night.
3. Based on the latest orbit solution of Dimorphos, data taken within mutual events were masked out.
4. Lightcurves were converted to differential magnitudes by subtracting off the mean magnitude outside of the masked mutual events. This zero-point offset was included as a fit parameter for each individual lightcurve.
5. A linear trend was fit to each lightcurve to correct for time-variable brightness of ejecta within the photometric apertures.
6. The primary rotational signatures in the differential corrected lightcurves were fit with Fourier series based on data points outside of mutual events.
7. The Fourier fits were subtracted off of the differential lightcurves to generate residuals that isolated the mutual events.
8. The rms of the residuals outside of mutual events was calculated to assess the quality of each decomposition.

An example of a single decomposed lightcurve from the LDT on 2023 February 21 is shown in Figure 3.

The decomposition process began with light-time correction so that all measurements were tied to the reference frame of the asteroid. We adopted a simple first-order (noniterative) light-

time correction by subtracting Didymos’s topocentric distance divided by the speed of light from the JD times of observation. Iterative corrections accounting for the motion of Didymos during this light travel time interval were not applied. These first-order corrections ranged from about 4 minutes down to 30 s at closest Earth approach in early October. Based on the motion of Didymos, subsequent iterative corrections would have been at least 3 orders of magnitude smaller and thus insignificant relative to individual exposure times and features in the lightcurve.

Within each observing session, the viewing geometry—characterized by solar phase angle, geocentric range, and heliocentric distance—changed slightly, which caused small monotonic changes in brightness. We corrected for this by retrieving with the Python *astroquery* package an ephemeris for Didymos from JPL Horizons. Horizons calculates ephemerides using the *HG* magnitude system (Bowell et al. 1989) and used values of  $G = 0.15$  and  $H = 18.12$  for Didymos. We used this ephemeris to compute differential changes in magnitude relative to the mean. Those differential changes were applied to each measured lightcurve independently. Though we show in Section 7 that an *HG* model does not provide the best fit to the entirety of the postimpact photometry, these geometry-dependent magnitude corrections were so small ( $<0.1$  mag for each lightcurve) that differences in photometric models or specific *HG* parameters were insignificant to the decomposition process.

To properly fit the rotational signature of Didymos, we had to identify and mask out portions of each lightcurve that were taken during mutual events (Figure 3). This masking was critical to ensure that the Fourier fit to the rotational lightcurve of Didymos was not affected by mutual events. Defining masks was straightforward prior to impact because the orbit of Dimorphos was well constrained (Naidu et al. 2022; Scheirich & Pravec 2022). After DART impact, a new orbit solution was found within the first 2 days (Thomas et al. 2023), again allowing for identification of mutual events. However, the postimpact orbit solution continued to get refined throughout the apparition. Our mutual event masks thus reflected the most current orbit solution with an additional buffer of up to 0.025 day (36 minutes) at the beginning and end of each event to account for uncertainties in event predictions. With these masks defined, we converted our lightcurves to differential magnitudes by subtracting off mean magnitudes outside of mutual events.

A final correction was applied to each lightcurve to account for the changing brightness of impact ejecta within photometric apertures. Originally, this was conceived as a way to compensate for fading of ejecta as it escaped the system. These were small corrections, applied to account for measured ejecta fading rates of  $\sim 0.1$  mag day<sup>-1</sup> (e.g., Graykowski et al. 2023). So for a typical lightcurve, this involved a linear correction of no more than a few hundredths of a magnitude across the observing session. However, given the heterogeneity of the overall data set, it was not possible to disentangle this slope correction from other observational issues, such as variable extinction or seeing effects. Furthermore, it was found that the ejecta were not simply fading in a monotonic fashion. Instead, there is clear evidence of complex variability in ejecta brightness. For example, secondary collisions may have produced an increase in ejecta about 8 days after impact (see Section 7 and Kareta et al. 2023). As such, we allowed the

**Table 3**  
Lightcurve Decompositions from the 2022–2023 Observations

ID	JD Range	Points	Lightcurves	Fit Order	rms
Pre-L1	2459762.6669 – 2459767.9728	706	5	9	0.0067
Pre-L2	2459791.6504 – 2459791.9057	125	1	10	0.0080
Pre-L3.1	2459809.5313 – 2459810.7136	229	2	12	0.0132
Pre-L3.2	2459813.5676 – 2459817.5414	2135	7	9	0.0097
Pre-L3.3	2459821.5357 – 2459824.9126	2123	4	9	0.0084
Pre-L3.4	2459826.5995 – 2459828.6771	286	3	9	0.0066
Pre-L4.1	2459834.5636 – 2459838.9102	1031	6	9	0.0091
Pre-L4.2	2459840.8258 – 2459844.9064	1248	7	11	0.0066
Pre-L4.3	2459845.7830 – 2459848.8959	2610	9	9	0.0070
L0.1	2459850.6063 – 2459850.8867	577	2	7	0.0066
L0.2	2459851.6116 – 2459851.8663	1284	3	10	0.0053
L0.3	2459852.5897 – 2459852.8888	1675	6	11	0.0058
L0.4	2459853.4068 – 2459853.8951	1362	5	12	0.0044
L0.5	2459854.4089 – 2459854.9549	1595	5	11	0.0052
L0.6	2459855.4172 – 2459855.7280	1238	6	11	0.0046
L0.7	2459856.5925 – 2459856.8663	657	4	11	0.0053
L0.8	2459857.4693 – 2459857.7773	774	5	10	0.0066
L0.9	2459858.4297 – 2459858.8509	1214	5	9	0.0057
L0.10	2459859.6737 – 2459859.8807	712	3	9	0.0062
L0.11	2459860.4382 – 2459860.8954	805	3	10	0.0070
L0.12	2459861.4424 – 2459861.8936	837	4	9	0.0069
L0.13	2459862.6761 – 2459862.7933	767	3	12	0.0083
L1.1	2459869.6181 – 2459870.0207	165	2	9	0.0100
L1.2	2459872.8759 – 2459874.0173	374	3	11	0.0085
L1.3	2459876.8377 – 2459880.0287	666	8	9	0.0094
L1.4	2459880.5413 – 2459886.0129	1455	14	14	0.0094
L2.1	2459900.7059 – 2459901.7576	715	4	9	0.0065
L2.2	2459901.8103 – 2459904.0346	986	6	10	0.0074
L2.3	2459904.5753 – 2459907.0441	1019	9	12	0.0067
L2.4	2459907.7170 – 2459909.0380	817	8	13	0.0077
L2.5	2459909.7477 – 2459911.5513	492	5	13	0.0072
L2.6	2459911.4180 – 2459913.9069	1176	10	12	0.0084
L2.7	2459914.6155 – 2459915.9442	647	6	12	0.0065
L3.1	2459927.9180 – 2459929.0688	713	2	14	0.0050
L3.2	2459930.4872 – 2459931.0263	300	3	14	0.0064
L3.3	2459932.4297 – 2459934.9537	1035	10	12	0.0091
L3.4	2459935.2858 – 2459937.5623	448	4	13	0.0093
L3.5	2459938.0873 – 2459940.3691	1036	7	13	0.0101
L3.6	2459941.4396 – 2459944.8952	415	4	11	0.0060
L4.1	2459955.5764 – 2459962.7933	501	6	11	0.0082
L4.2	2459968.5436 – 2459974.7416	1058	10	12	0.0098
L5.1	2459986.5711 – 2459986.9064	255	1	11	0.0079
L5.2	2459992.6056 – 2460000.8285	269	4	11	0.0059
Totals:		38,532	224		

**Note.** The columns correspond to the ID for each decomposition, the range of JD dates associated with the data, the number of data points and lightcurves in each decomposition, the order of Fourier series used to fit the primary lightcurve, and the rms associated with those fits.

slope correction to vary from  $-0.25$  to  $+0.25$  mag day $^{-1}$  for all data sets. This decision was supported by lower rms values in the final decompositions when these slope corrections were applied.

With the differential, fully corrected lightcurves, we fit the data for each decomposition with a Fourier series of the form

$$m(t) = \sum_{n=1}^k \left[ A_n \cos \frac{2\pi n}{P}(t - t_0) + B_n \sin \frac{2\pi n}{P}(t - t_0) \right] - \beta(t - t_0) + \delta m, \quad (1)$$

where  $m(t)$  is the differential magnitude at time  $t$ , the sum over  $n$  defines the order  $k$  of the Fourier series,  $A_n$  and  $B_n$  are the Fourier coefficients,  $P$  is the rotation period of Didymos

( $=2.2600$  hr; Pravec et al. 2006),  $t_0$  is the start time of the lightcurves included in each decomposition set,  $\beta$  is the slope parameter in the range  $-0.25$  to  $0.25$  mag day $^{-1}$  correcting for monotonic variability of the ejecta, and  $\delta m$  is a small differential offset applied to each lightcurve individually to minimize the rms in the final decomposition. This formalism is similar to previous works (e.g., Pravec et al. 2000, 2006, 2022) but does differ slightly. For simplicity, we fit the measured magnitudes as opposed to converting and fitting units of flux. We found that the quality (rms) of the Fourier fit was identical when fitting fluxes or magnitudes. Fitting in logarithmic (magnitude) space was likely adequate for these data because of the relatively low amplitude of the lightcurves. We also did

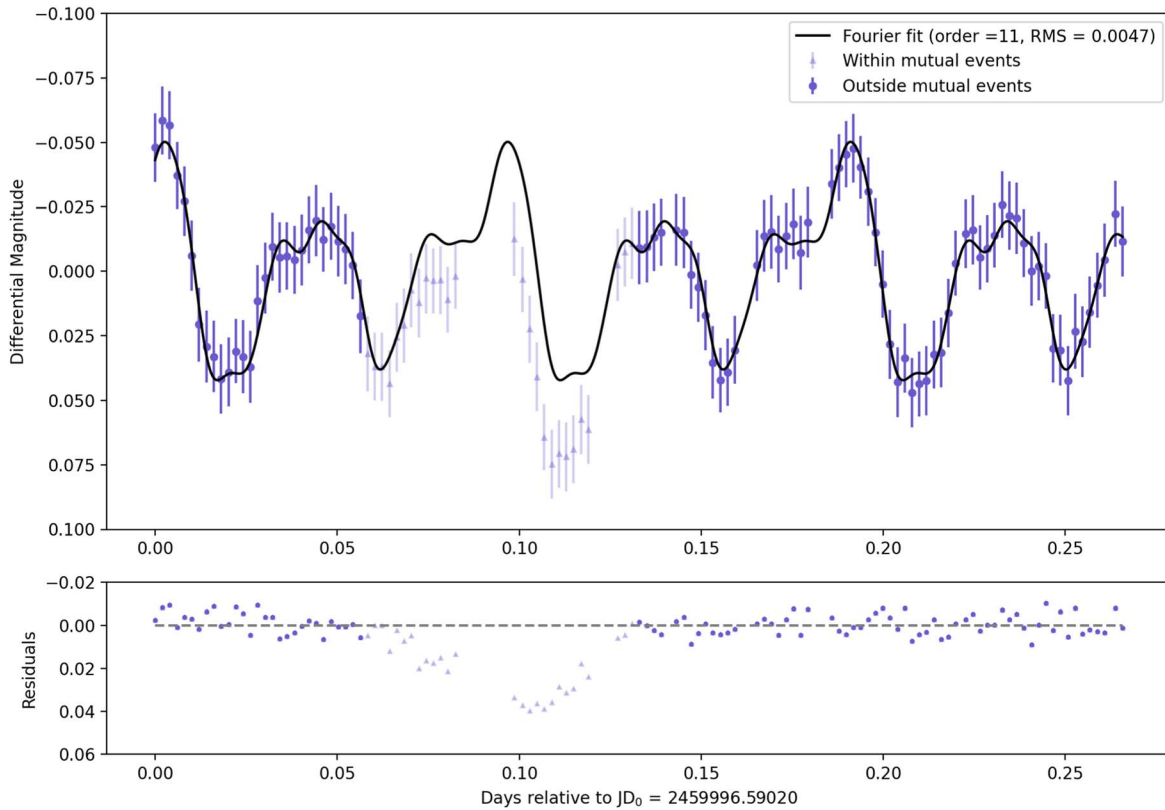


**Figure 3.** Light-time and geometry-corrected differential lightcurve measured on 2023 February 21 from the LDT (top). This lightcurve was part of the L5.2 decomposition. The Fourier fit to the differential lightcurve was subtracted off the measured signal to produce residuals that isolated a primary eclipse and occultation centered around  $t = 0.1$  days (bottom). The low rms of the fit ( $=0.0047$ ) and relatively flat residuals outside of the mutual event are indicators of a clean decomposition. The reported photometric error bars in the top panel were ignored when fitting the Fourier series.

**Table 4**  
Data from the DART Lightcurve Campaign

JD	Mag.	Differential mag.	Residual mag.	Run ID	Decomposition ID
2459762.66372	18.752	-0.010	0.0051	Magellan_2022-07-02	Pre-L1
2459762.66520	18.764	0.002	0.0104	Magellan_2022-07-02	Pre-L1
2459762.66661	18.754	-0.008	-0.0017	Magellan_2022-07-02	Pre-L1
2459762.66955	18.742	-0.019	-0.0018	Magellan_2022-07-02	Pre-L1
2459762.67097	18.763	0.002	0.0290	Magellan_2022-07-02	Pre-L1
...					

(This table is available in its entirety in machine-readable form.)

not explicitly fit a mean magnitude term in Equation (1). This is because this equation was applied to differential lightcurves normalized by their individual means and offset with the small  $\delta m$  corrections, typically  $<0.01$  mag. Given the heterogeneity of our data set in terms of filters and calibration techniques, fitting to a mean magnitude would not have been beneficial. We also did not include a term for the rotational signature from Dimorphos. That analysis is saved for future work.

A “curve-of-growth” approach was employed to determine the optimal Fourier order (Table 3). A range of orders  $k$  from 5 to 15 were scanned, with the optimal fit corresponding to the  $k$  value for which the rms on individual lightcurves changed by  $<0.001$  mag. The period of the primary  $P$  was held constant throughout the apparition, as there was no clear evidence that the rotation period of Didymos was changed significantly by the DART impact.

The final residuals and rms values were determined by subtracting the Fourier fit from all lightcurves in a decomposition set. The rms was computed based on residuals outside of mutual events (Figure 3). Attempts to compute formal chi-squared statistics were less useful than rms because of the inconsistency in which error bars were reported on the measured photometry. Some data sets had significantly overestimated errors, while others were significantly underestimated. Lacking a way to homogenize the error bars, we simply ignored them in the fitting process and computed the rms residuals to assess the data quality of individual lightcurves.

The process to generate sets of decomposed lightcurves was highly iterative, involving regular adjustments when new data were added or reductions were updated. The overall rms residuals, as well as the rms values associated with individual lightcurves, were used to reject or accept data. On average, rms residuals  $<0.015$  mag were required for acceptance.

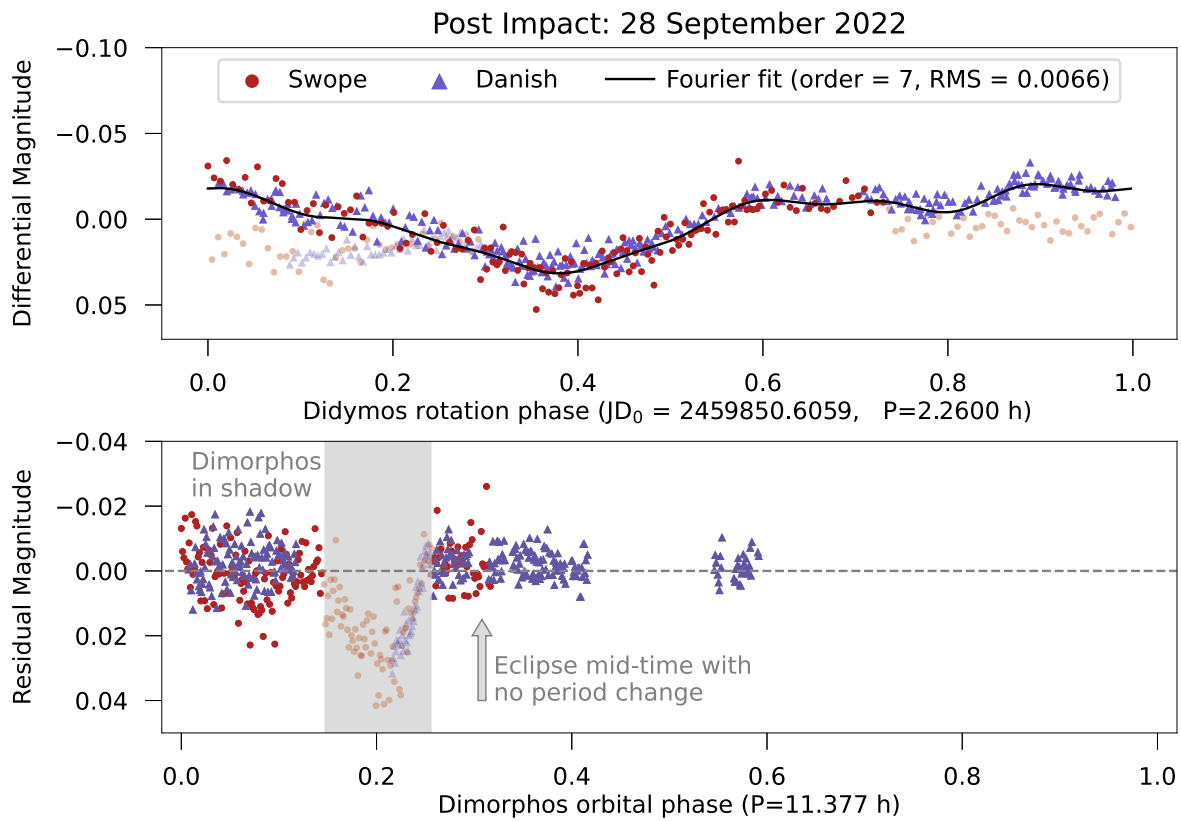


**Figure 4.** The first mutual event after DART impact was detected in lightcurves from 2022 September 28, only  $\sim 29$  hr after impact. This event was observed by the Swope (red) and Danish (blue) telescopes. Faded points correspond to data taken within the mutual event. Decomposition of these lightcurves (bottom) revealed a secondary eclipse clearly offset in time relative to an unperturbed orbit solution (gray arrow). This offset of about 1 hr, measured after Dimorphos completed two postimpact orbits, provided the first indication in lightcurves for the 33 minute orbit period change (Thomas et al. 2023).

Exceptions were made, for example, if a noisier lightcurve covered key rotational phases not represented by other lightcurves. Generally, the range of dates for each decomposition set was defined when changes in the morphology of the primary lightcurve exceeded  $\sim 0.015$  mag. This led to many individual decompositions around the time of closest Earth approach (lunation L0), when the viewing geometry to the system changed fastest, and longer decomposition intervals at the beginning and end of the apparition (Table 3). Other factors that were included in this iterative process included the order of the Fourier series, the start and end times of mutual events (based on ephemeris updates), the zero-point offsets for each individual lightcurve, and the slope parameter used to account for time-variable ejecta.

## 5. Decomposition Results

The full suite of lightcurve data and decompositions is included with this manuscript as a supplementary data file; a representative subset of these data is shown in Table 4. The columns in the table are light-time corrected Julian Date; measured apparent magnitude; differential magnitudes that have been geometry-corrected, slope-corrected, mean subtracted, and zero-point offset (Section 4); decomposed residuals, which are the differential magnitudes with the Fourier fits subtracted off; and IDs for the observing runs and decompositions. The combination of run and decomposition IDs (Table 3) provides a unique mapping to each individual lightcurve. The run ID indicates the observatory and UT date associated with the start time of each lightcurve

and map to the observational details in Table A1. In some cases an observatory may have contributed two lightcurves from the same UT date (e.g., LCOGT data from 2022 September 12), in which case the letters “a” and “b” were appended to the run IDs to distinguish them as distinct. The full suite of data in the machine-readable table (see Table 4) is organized in chronological order with each lightcurve presented as an uninterrupted block. This data file does not include an indication of which data points were measured within mutual events. Computed beginning and end times for mutual events based on the two independent orbital models (Naidu et al. 2023; Scheirich et al. 2024) are included with those publications. Those event time predictions can be combined with the data provided here for future analyses.

The decomposed residuals from the 2022–2023 campaign provided a foundation for determining the pre- and postimpact orbit of Dimorphos (Thomas et al. 2023). Immediately following DART impact, the expectation was that mutual events might not be detectable with lightcurves for days or even weeks due to obscuration by ejecta (Fahnestock et al. 2022). Fortunately, continued observations during this time revealed the first postimpact mutual event just  $\sim 29$  hr after impact (Figure 4). A few assumptions facilitated the identification of this event. First, the head-on geometry of the spacecraft impact suggested that the orbit period of Dimorphos would decrease from its preimpact value of 11.92 hr. Second, models predicted likely values for  $\beta$  of 1–5 (Stickle et al. 2022), which translated to a period change of about 10 minutes up to 1 hr (Meyer et al. 2021). Third, the known geometry of the system (Naidu et al. 2022; Scheirich & Pravec 2022) suggested that



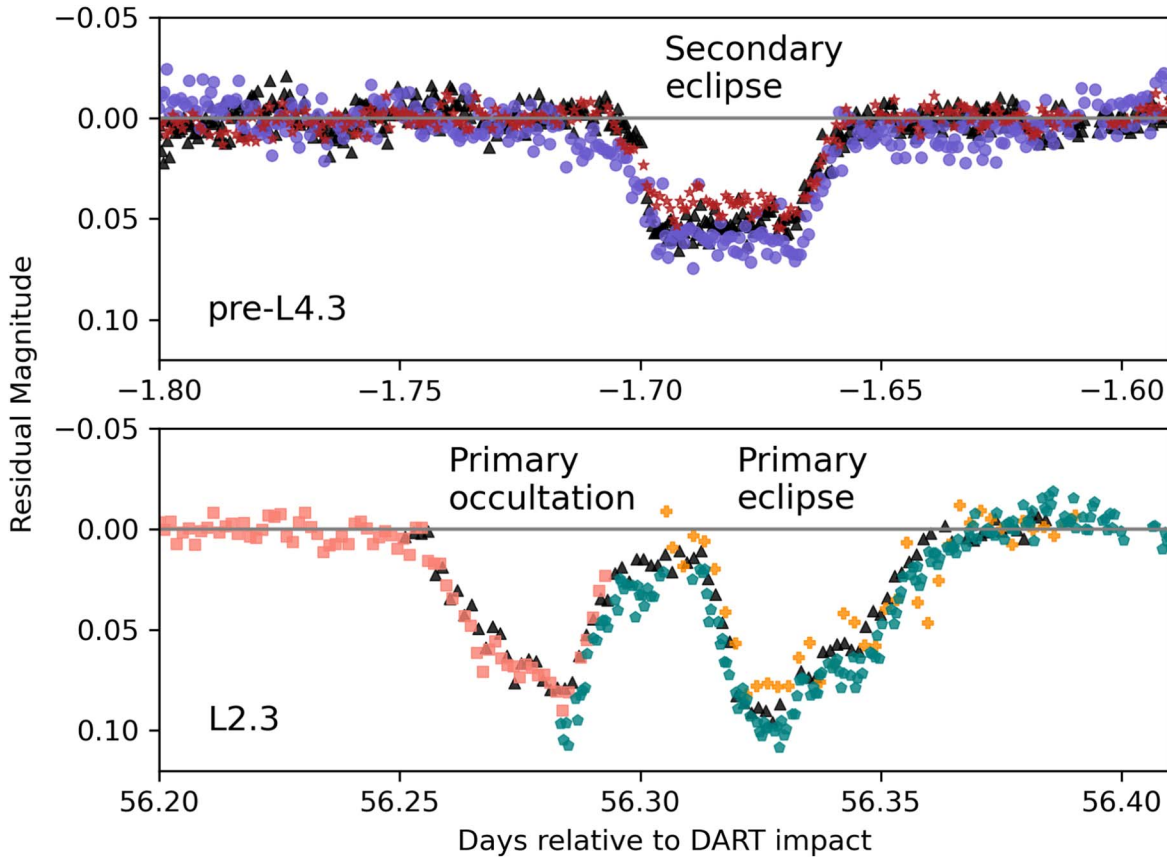


**Figure 5.** Examples of secondary (top) and primary (bottom) mutual events that were simultaneously sampled by more than one observatory. The top and bottom panels correspond to the preimpact L4.3 and postimpact L2.3 lunations, respectively. These data demonstrate the high precision achieved with these observations, generally 0.01 mag or better, and the good agreement across facilities and reduction methods. The key for these points is: 1 m Swope = blue circles, 0.6 m TRAPPIST = red stars, 1.5 m Danish = black triangles, 1 m LCOGT = salmon squares, 1.1 m Hall = orange plus signs, and 2.4 m MRO = teal pentagons. Visualization of the system at specific mutual event geometries (e.g., onset of primary occultation) is shown in Naidu et al. (2023).

secondary eclipses in late September would last for about an hour. Based on these expectations, we attempted to decompose the immediate postimpact lightcurves with mutual event masks that spanned a plausible range of new orbital periods. In particular, we applied a 1 hr mask across a range of orbit periods from 11 to 12 hr in steps of 0.1 hr. This period scan revealed a secondary eclipse in data from UT 28 September that corresponded to a new orbit period of around 11.4 hr (Figure 4). The depth of this mutual event was about 0.03 mag, or 60% of that predicted by the models of Scheirich & Pravec (2022). This suggested, unsurprisingly, that the increased flux from residual ejecta muted the depth of this mutual event. In Section 6, we explore how the depth of mutual events evolved as ejecta cleared out of the system.

A wide variety of mutual events were seen as the viewing geometry of the Didymos system changed throughout the 2022–2023 apparition. This variety included discrete (separated in time) primary and secondary eclipses and occultations, as well as events that overlapped in time. In some cases, events were covered simultaneously by multiple observatories (Figure 5). These simultaneous observations provided important consistency checks across facilities and data reduction methods. Typically, the data were consistent at the level of  $\sim 0.01$  mag. Comparing simultaneous observations also helped to highlight sections within individual data sets that may have had reduction problems and thus could not be accepted as part of the final data set.

In general, these decomposed residuals provided the best means for validating and accepting individual lightcurves. The full lightcurve data set demonstrated high data quality (e.g., accuracy and precision of  $\sim 0.01$  mag) sustained over an 8 month observing window, with some individual lightcurves meeting these standards for more than 8 hr in a single night (Table A1).

## 6. Mutual Event Depths

With nearly 8 months of data spanning the impact apparition, we assess the evolution of mutual events relative to models. Such models, e.g., Naidu et al. (2022) and Scheirich & Pravec (2022), have been well demonstrated to reproduce the timing of mutual events. Here we focus on the predicted depths of mutual events relative to the data. We approach this comparison cautiously because these models were not explicitly developed to match the detailed shapes of mutual events. Factors such as topography, nonuniform albedo, or photometric scattering properties could all have contributed to discrepancies between the data and model. We discuss these complications further in Section 9.

The details of the photometric model used for this analysis are presented in Naidu et al. (2023). This model was primarily developed to facilitate improved measurement of mutual event times from decomposed lightcurves and thus served the mission’s level 1 requirement of measuring the period change. This model used rotationally symmetric ellipsoid shapes for Dimorphos and Didymos based on the extents reported by

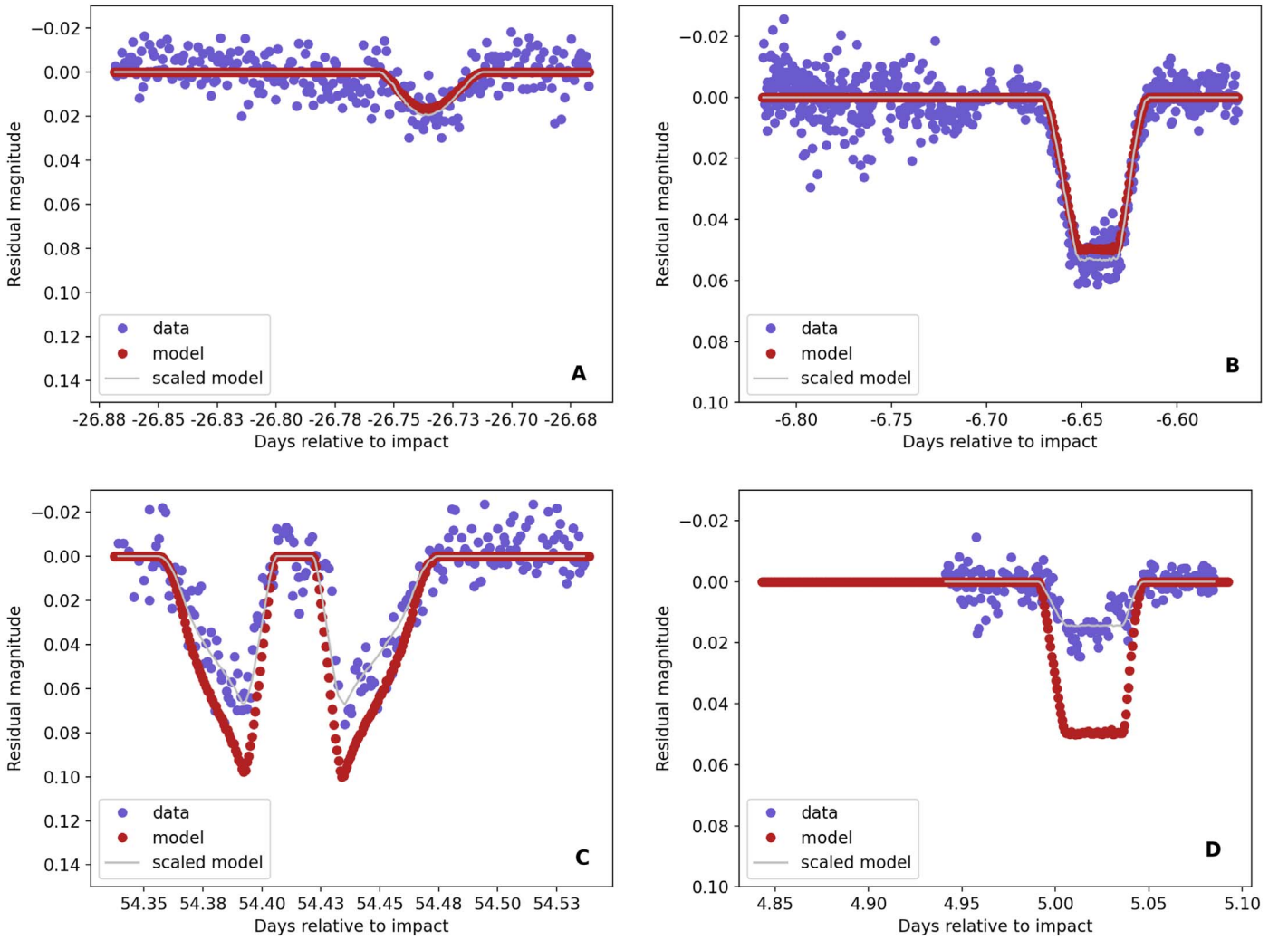


**Figure 6.** Select mutual events from the preimpact (panels (A) and (B)) and postimpact (panels (C) and (D)) data. Panel (A) is a primary eclipse, panel (B) a secondary eclipse, panel (C) shows both a primary eclipse and primary occultation, and panel (D) is a secondary eclipse. The mutual event models of Naidu et al. (2023) are overplotted. In all cases, the models are multiplicatively scaled to determine a best fit to the data. In the postimpact data ((C) and (D)), the models overpredict the depth of mutual events, a difference that can be attributed to the effects of residual ejecta in the system. Visualization of the bodies in specific mutual event configurations is presented in Naidu et al. (2023).

Daly et al. (2023), though the dimensions of Dimorphos were scaled up by 10% to calibrate against preimpact mutual event data. The photometric model used the latest orbit solution for Dimorphos (Naidu et al. 2023) and, for simplicity, treated the net photometric signature of the system assuming the Lommel–Seeliger (LS) law for diffuse scattering (e.g., Kaasalainen & Torppa 2001). LS parameters were adopted to be representative of S-type asteroids (Huang et al. 2017). This model produced realistic predictions for both the timing and morphology (shape and depth) of mutual events. Figure 6 shows this model as compared to select mutual events in pre- and postimpact lightcurves. In these cases, it is clear that the timing and qualitative shape of the events are well represented by the models. However, the depths of events in the postimpact data are sometimes shallower than model predictions. This can be attributed to the influence of residual ejecta in the system.

With ejecta present, the observed depth of mutual events in magnitudes can be expressed as

$$m_{d,\text{obs}} = -2.5 \log \left( \frac{(f_P + f_s - \Delta f) e^{-\tau} + f_e}{(f_P + f_s) e^{-\tau} + f_e} \right), \quad (2)$$

where  $f$  is the flux from the primary Didymos ( $P$ ), secondary Dimorphos ( $s$ ), or ejecta ( $e$ ); the change in brightness due to a mutual event is  $\Delta f$ ; and extinction from the surrounding ejecta is characterized by attenuation of flux for optical depth  $\tau$ . The modeled mutual event depths ( $m_{d,\text{model}}$ ) did not include the extinction ( $e^{-\tau}$ ) or ejecta ( $f_e$ ) terms in Equation (2). Thus, when the ejecta is optically thick (i.e.,  $\tau \sim 1$ ) or contributing significant flux, we expect the model and data to show significant differences.

We estimate the difference in magnitude between the model and observations,  $\Delta M = m_{d,\text{model}} - m_{d,\text{obs}}$ , by minimizing the rms between the data and scaled versions of the model (e.g., Figure 6). This was done for all mutual events in the data set. For each event, we scanned a range of multiplicative scaling factors from 0.01 to 2.0 in steps of 0.01 to find the minimum rms. For each mutual event, the value for  $\Delta M$  was then the difference in minimum brightness (maximum magnitude) of the nominal model relative to the scaled model. With this approach, we determined that the first mutual events after impact were  $\sim 0.04$  mag shallower than predicted by the models. If we assume (incorrectly) that this difference is

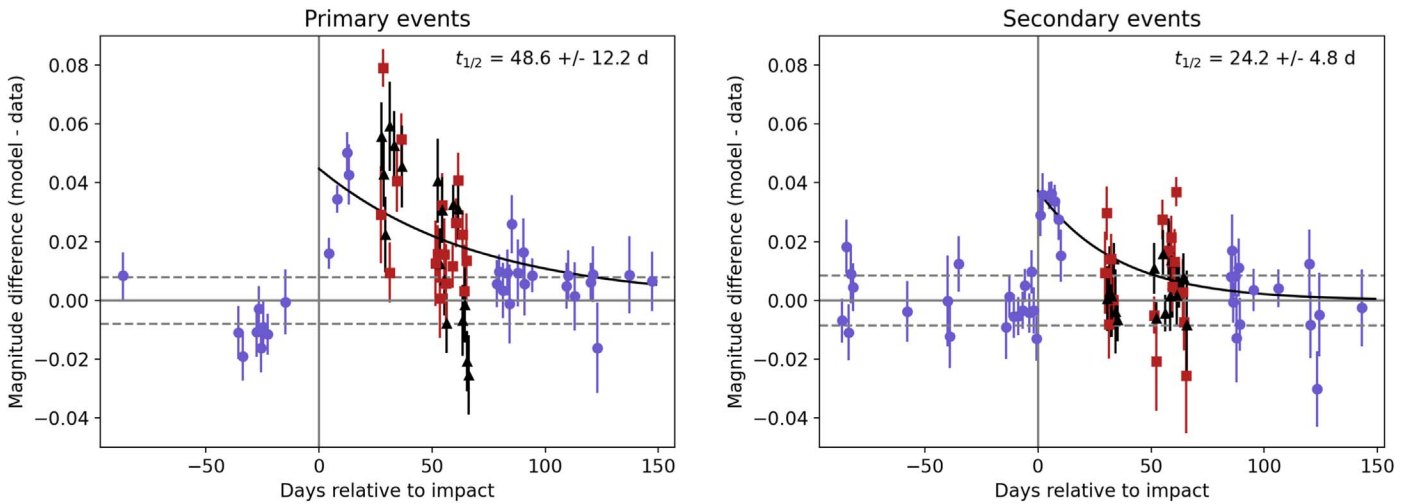


**Figure 7.** Difference in magnitude  $\Delta M$  between modeled and observed mutual event depths. The events prior to impact provided a baseline for the expected variance, i.e., how well the model represented the data. Increased positive differences after impact (vertical line) are due to the influence of ejecta on the observations. The horizontal dashed lines are  $\pm 1\sigma$  of the preimpact values. The error bars on the points are the rms associated with the scaled models that best fit the data. Exponential decay curves (black lines) were fit to the postimpact points. Between 26 and 67 days after impact, eclipses (black triangles) and occultations (red squares) were temporally separated and thus could be independently fit. All other points (blue circles) represent either single events or blended eclipses and occultations.

exclusively due to extinction by the surrounding ejecta, i.e., flux from the ejecta  $f_e$  can be ignored, and that the observed flux is simply  $f_{\text{model}} \times e^{-\tau}$ , then standard relationships between optical depth and extinction suggest  $\tau = \frac{\Delta M}{1.086} \sim 0.04$ . It is thus clear that the ejecta became optically thin within the first day or so after impact.

For a period of about 6 weeks in late 2022 (lunations L1 and L2), when Didymos was at relatively high solar phase angles  $\alpha$ , eclipses and occultations were separated in time (Figure 6(C)). In our data, this separation was apparent from October 24 ( $\alpha = 76^\circ$ ) to December 2 ( $\alpha = 46^\circ$ ). In this window, we were able to independently assess the model fit to occultations and eclipses. Outside of this window, occultations and eclipses overlapped in time, and we thus computed a single best-fit scaling factor that did not consider the events separately.

The model versus observed event depths were used to characterize the timescale on which the ejecta dissipated (Figure 7). Prior to impact, variations in  $\Delta M$  provided a quantitative assessment of how well the model represented the data. For both primary and secondary events, the standard deviation for  $\Delta M$  was  $\sim 0.01$  mag, suggesting that this is the noise floor below which we were unable to resolve meaningful signatures due to combined uncertainties in the data, the lightcurve decomposition process, and the mutual event models. This floor is consistent with our data quality requirements for accepted lightcurves (Section 4).

After impact, there was a clear signature of positive  $\Delta M$  that then gradually decayed. We treated the  $\Delta M$  values for primary and secondary events separately and independently fit them with exponential decay curves. Both decay curves show initial values around 0.04 mag. Of course, this “initial” value is tied to the first postimpact mutual event, which was not detected until 29 hr after impact. Lightcurves collected  $< 29$  hr after impact were not decomposable and thus not considered here.

Surprisingly, the primary and secondary events displayed different  $\Delta M$  decay profiles. We found that the  $\Delta M$  half-life for secondary events was  $24.2 \pm 4.8$  days, fully consistent with the bulk photometric fading of 23.7 days presented in Graykowski et al. (2023). However, the corresponding

timescale for primary events was longer at  $48.6 \pm 12.2$  days. The primary decay curve also did not return to zero at the end of the apparition but instead remained slightly offset by  $\sim 0.01$  mag. It seems implausible that ejecta would still be affecting event depths 5 months after impact. The reasons for these issues are not obvious, but we do discuss possibilities below that motivate avenues for future work. Regardless of the cause(s) of these offsets in event depth, the close correspondence between data and model in event timing and general morphology suggests that macroscopic ejecta like the boulders seen in Hubble Space Telescope images (Jewitt et al. 2023) or optically thick clouds did not contribute significantly to the mutual event signatures.

## 7. Photometric Fading of the System

Several facilities that contributed to the lightcurve campaign collected data for 3–4 months after impact. These extended data sets provided a means to monitor fading of ejecta and the photometric phase curve of the system (Figure 8). Our aim here is to address two questions: when does ejecta no longer contribute significantly to the bulk photometry, and do standard photometric models represent the photometric behavior of the system? More details on photometric modeling of ground-based and in situ data are presented in Hasselmann et al. (2023). In this analysis, we focused on three data sets: those from the Lowell Observatory 1.1 m, the Danish 1.5 m, and the dual TRAPPIST 0.6 m telescopes. Each of these data sets were independently reduced using different methods (Section 3), but internally, they adopted uniform approaches across the full postimpact window and thus represent a consistent and well-calibrated baseline for long-term photometric characterization. All of the Lowell photometry was measured with a  $5''$  aperture, the TRAPPIST data with a  $7''.2$  aperture, and the Danish data with a  $2''.5$  aperture. For each night of observation, the mean magnitude outside of mutual events and mid-JD are plotted in Figure 8. These averages compensate for lightcurve variability.

Filter transforms were required to compare these data. The Lowell observations were obtained with a broad VR filter and calibrated to PanSTARRS  $r$ . The Danish data were obtained in

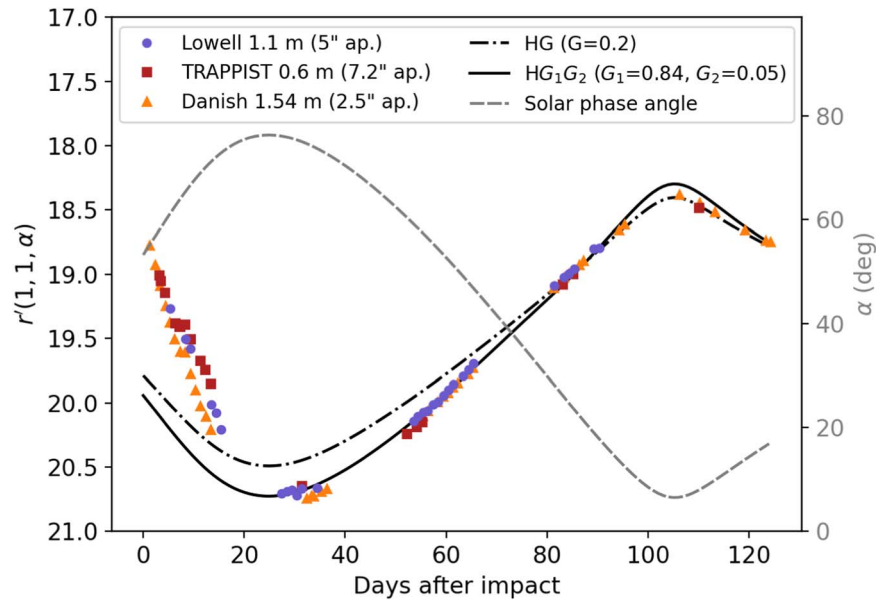


**Figure 8.** Apparent  $r$ -band magnitudes, normalized to geo- and heliocentric ranges of 1 au, of the Didymos system after DART impact. These curves include both phase angle effects and fading of ejecta. All magnitudes have been converted to the PanSTARRS  $r$  filter (see text for details). Three data sets are shown: Lowell 1.1 m (blue circles), TRAPPIST 0.6 m (red squares), and Danish 1.54 m (orange triangles). The photometric aperture for each data set is given in the legend. Both  $HG$  (Bowell et al. 1989) and  $HG_1G_2$  (Muinonen et al. 2010) photometric models are plotted in black. The solar phase angle  $\alpha$  (dashed gray curve) spans a wide range of values from a maximum of  $76^\circ$  down to a minimum of  $6^\circ$ .

Johnson–Cousins  $V$  or  $R$  and calibrated to Cousins  $R$ . The TRAPPIST data were obtained with the broad Exo filters and calibrated to Cousins  $R$ . All data were converted to the PanSTARRS  $r$  bandpass. These conversions were based on the measured  $B - V = 0.795$  and  $V - R = 0.458$  colors of Didymos from Kitazato et al. (2004). The former was used to compute  $V - r = 0.22$  based on the transforms of Jester et al. (2005), which then gives  $R - r = -0.24$ . These colors were also used to estimate the absolute magnitude for Didymos. The mission-adopted  $V$ -band absolute magnitude  $H_V = 18.16$  (Pravec et al. 2012) converts to  $H_r = 17.94$ , which we use below to compute the photometric phase function.

A few nonuniform aspects of these data are noted. The photometric aperture for each data set was different. This produced a clear trend in brightness as a function of aperture size, which was also discussed in Kareta et al. (2023). The data with the smallest aperture (from the Danish) appear systematically fainter, and the data with the largest aperture (from TRAPPIST) were systematically brighter. However, these are relatively small effects, most pronounced in the first 20 days after impact when significant ejecta was still present, and do not significantly influence the broad conclusions made here.

We have also added 3 nights of data, UT October 10, 11, and 12 (impact +13 to +15 days), from the Lowell 1.1 m that were not included in the lightcurve analysis (Section 4). These data were not viable for lightcurve decomposition, but the mean magnitudes they provide are consistent with general trends and provide temporal sampling on days without other data.

The curves in Figure 8 correspond to apparent magnitudes normalized to geocentric and heliocentric ranges of 1 au and thus still include the effects of changing solar phase angle and the influence of ejecta on the total brightness of the system. This facilitates comparison to photometric phase curves computed in the convention of the IAU  $HG$  system (Bowell et al. 1989) and the  $HG_1G_2$  system (Muinonen et al. 2010). The value  $G = 0.2$  from Kitazato et al. (2004) is used for the  $HG$

calculation. Values of  $G_1 = 0.84$  and  $G_2 = 0.05$ , derived from fits to LICIAcube, DRACO, and ground-based data (Hasselmann 2023), were used for the  $HG_1G_2$  model. These particular  $G_1$  and  $G_2$  values are unusual, but not unprecedented, for S-type asteroids (Penttilä et al. 2016; Mahlke et al. 2021).

The comparison of our data to these phase curves highlights several key results. First, all three data sets confirm an inflection in fading rates starting about 8 days after impact (Kareta et al. 2023). This “8 day bump” is not a result of changing viewing geometry but may be due to increased ejecta following secondary impacts in the system. Second, the  $HG$  model does not represent the data well at phase angles  $>30^\circ$ , suggesting that estimates of the system brightness relative to  $HG$  predictions would be off by up  $\sim 0.2$  mag in the 2 months following impact. The predicted  $HG$  magnitudes do represent the data well later in the apparition (lunations L3 and L4), when ejecta no longer dominated the photometric signal and phase angles were lower. Finally, we estimate that the system returned to preimpact brightness about 20 days after impact. Analysis of other data sets taken in the 16–26 day window after impact, e.g., like those presented in Graykowski et al. (2023) and Kareta et al. (2023), provide additional insights into when the ejecta no longer contributed a detectable enhancement. For the data presented here, interpolation from 1 to 15 days shows a return to the  $HG_1G_2$  model around 20 days postimpact.

## 8. Tail Persistence

All lightcurves presented here (and even those from 2023 March that could not be used for decomposition analysis) were collected and decomposed with a tail still present. Even though the system returned to preimpact brightness within about 20 days, the tail persisted for the entirety of the apparition with gradually decreasing brightness. While the lightcurves clearly measured the mutual events with sufficient precision to conduct the analyses described elsewhere in this paper, the



**Figure 9.** Comparison of the relative brightness of the tail in five stacked images from SOAR and the LDT spanning from 2022 September 28 through 2023 January 25. All images utilize the Sloan  $r$  filter, go to approximately equal depths, and are scaled logarithmically between the peak brightness of the central condensation and 0.5% of that value.

interpretation of our results still depends on the influence that the tail and other ejecta played in the measured photometry.

In Figure 9, we showcase five identically scaled image stacks of the Didymos system in the first 4 months after impact. The tail was still detectable from 4 m class telescopes an appreciable fraction of a year after impact, far beyond expectations, but it also dimmed significantly over that time period. As mentioned in Section 7, the system returned to its preimpact brightness within several weeks of impact, suggesting that the tail (and ejecta broadly) contributed negligible brightness after that period despite its continuing detectability. The persistence of the primary tail over such a long period implies ongoing escape of ejecta for many months after impact, and its gradual decline in brightness (optical thickness) suggests that mass loss at increasingly small rates continued well after the tail was no longer contributing significant photometric signal.

To estimate this small contribution and compare it against other quantities, like the mutual event depths, we follow a procedure outlined in Sanchez et al. (2019). In essence, the brightness profile of the tail as a function of distance from the optocenter is fit well away from the central point-spread function and then extrapolated inward toward the optocenter. This results in an estimate of the fraction of the brightness in the central few pixels that may be attributed to the tail. There are several caveats to this methodology that are worth noting, primarily driven by assuming that the structure of the tail thousands of kilometers from the asteroids can be extrapolated meaningfully inward. For example, dust passing behind the asteroids may not have been fully illuminated, or dynamical effects near the binary system may have caused the dust to not be uniformly distributed. Utilizing the images in Figure 9, the estimated contribution was as much as  $\sim 10\% \pm 1\%$  of the nuclear signal on 2022 September 28 but dropped to  $\sim 1\% - 3\%$  on October 21, with lower values thereafter. In other words, by the time the system returned to its bulk brightness, the contribution of the tail was similar to or smaller than typical observational errors. Furthermore, in the first few weeks after impact, where the brightness of the bulk ejecta was important, the tail was but a minor contributor. In short, the brightness of the tail played little role in the photometric conclusions drawn here, but the persistence of the tail was a clear sign of ongoing mass loss from and evolution of the system more broadly.

## 9. Results and Discussion

We have presented an overview of the lightcurve photometry campaign carried out in support of the DART mission. Data and analysis were presented from the impact apparition,

spanning roughly 8 months from 2022 July to 2023 February. This large data set included 224 lightcurves from 28 telescopes, over 38,000 individual exposures, and represented over 1000 hr spent targeting the Didymos system (Table 2). The duration and observing circumstances (e.g., Galactic latitude, decl., apparent magnitude) of this campaign necessitated a coordinated plan that leveraged telescopes across a wide range of aperture sizes and geographic locations (Figures 1 and 2). A series of 10 observing windows (lunations) were defined during the impact apparition (Table 1) to maximize data quality and establish times when data collection rates were expected to be highest, thus providing the best opportunity for yielding sets of decomposable lightcurves. A set of practice targets were defined prior to the start of the apparition as a way for observers to establish observing and reduction protocols on targets with similar observing circumstances (e.g., apparent magnitude, nonsidereal rates, lunar phase) to Didymos in the weeks following impact. These preparatory steps were important to achieve strict S/N requirements; the mean rms residual across the full data set was 0.0073 mag, with some individual lightcurves showing residuals better than 0.004 mag.

Each observer employed their own data reduction methods. This was an intentional part of the campaign to avoid introducing systematic errors that might arise from a single, uniform approach to data reduction. Given the volume of data, subtle differences in reduction methods were unlikely to have much influence on the end results. However, one consequence of this approach was that the error bars on the reported photometry were not mutually consistent. As such, we ignored the reported error bars in the decomposition analysis (Section 4) and assessed the quality of each lightcurve based on rms residuals relative to the best-fit Fourier models.

The full suite of lightcurves was divided into 43 decomposable sets (Table 3), where a set was defined based on constant morphology of the primary rotational signature from Didymos. For a given set, the decomposition process included light-time and geometric corrections, masking of data taken during mutual events, and then fitting data outside of the mask with an  $n$ th-order Fourier series to isolate dips in brightness associated with mutual events. Included in this data set is the first postimpact mutual event captured just 29 hr after DART impacted Dimorphos (Figure 4), as well as simultaneous coverage of some events by as many as four independent observatories. Consistency across these multiply covered events provides an important validation of data reduction methods (Figure 5). The decomposition of lightcurves into their constituent parts—primary rotation and mutual events—provided the foundation for modeling the rotational and orbital dynamics of the Didymos system (Naidu et al. 2023; Scheirich

et al. 2024). To encourage future work with these data, we have included a machine-readable table with the full set of lightcurve measurements and decomposed residuals; see Table 4.

We have leveraged select aspects of this data set to investigate the postimpact photometric evolution of the system. While the focus on mutual events has been to derive their timing to serve as a constraint on the orbital period of Dimorphos (Naidu et al. 2023; Scheirich et al. 2024), the depths of the events also contain information about the influence of ejecta on the measured photometry. To facilitate this analysis, we compare the measured depths of mutual events to model predictions by Naidu et al. (2023). This comparison shows that prior to impact, the model reasonably represents the timing, depth, and gross morphology of mutual events (Figure 6). However, after impact, the measured event depths are systematically shallower than predicted by models (Figure 7). This is a clear indication of additional flux from residual ejecta acting to dampen the event depths in the observations. An initial dampening of  $\sim 0.04$  mag for the first detected mutual event on 2022 September 29 shows that the ejecta cloud is already optically thin at that time. We also fit decay curves to the postimpact offsets in mutual event depths ( $\Delta M = \text{model} - \text{observation}$ ). Secondary eclipses and occultations show behavior consistent with other constraints (e.g., Graykowski et al. 2023; namely, the mutual event depths return to model predictions with a half-life of  $24.2 \pm 4.8$  days. However, interpreting the analysis of primary events is not as straightforward. Our analysis shows that the measured primary events do not return to the model at the end of the apparition. Furthermore, the decay timescale for primary events is longer at  $48.6 \pm 12.2$  days. These different outcomes for primary (Didymos) versus secondary (Dimorphos) mutual events may be due to a number of factors.

The apparent differences in the  $\Delta M$  curves could be simply attributed to uncertainties in the data relative to the parameters being fit. The reported uncertainties on the decay timescales are  $1\sigma$ ; thus, the two are distinct at only the  $1.4\sigma$  level. Also possible is that the assumption of exponential decay may not be a good representation for the complex evolution of ejecta in the system. That certainly appears to be the case for primary events where  $\Delta M$  is roughly constant across the first two postimpact lunations before dropping off in the third lunation,  $\sim 50$  days after impact (Figure 7).

Assumptions built into the mutual event model could also be affecting the  $\Delta M$  decay curves. Incorrect assumptions about the body shapes and/or surface properties like albedo and roughness would lead to discrepancies between the model and observations. The biggest offsets between the data and model are seen for primary events in the L1 lunation (Figure 7). These occur when the system is at its maximum solar phase angle,  $\alpha > 70^\circ$ . It is possible that assumptions about photometric scattering and projected shapes break down at such viewing geometries. However, it is unclear how such assumptions would have an asymmetric affect, e.g., different decay timescales in primary versus secondary events.

The  $\Delta M$  discrepancy could also be attributed to the fact that secondary events are easier to reproduce with these models because they are less sensitive to the detailed properties of Dimorphos. In other words, when Dimorphos is in total eclipse or occultation, it no longer contributes to the measured flux of the system, and thus its detailed properties do not influence predicted depths for secondary mutual events. However, during

primary mutual events, the detailed properties of Dimorphos could have a more significant influence based on the specific regions on the surface of Didymos that are being shadowed or blocked. This conceptual interpretation seems reasonable and suggests that the model of Naidu et al. (2023) more accurately predicted the photometric behavior of secondary mutual events.

Further work is clearly needed to investigate some of these details in the data, as well as assumptions built into the mutual event model. More stringent vetting of data to consider only the highest-quality detections that cover both ingress and egress at high temporal resolution could help to mitigate uncertainty and scatter in the comparisons to the model. The model itself makes assumptions about the body shapes and scattering properties. Evidence for postimpact modifications to the shape of Dimorphos (Naidu et al. 2023) could have a significant influence on both occultation and eclipse depths. These effects would be most pronounced at high solar phase angles (e.g., lunation L1), when occultations and eclipses were well separated in time and occurred many tens of degrees apart in the mean anomaly of Dimorphos. Higher-order dynamical effects such as libration and precession of Dimorphos (Naidu et al. 2023) could also be complicating the interpretation of the data. It is also possible that the assumed LS properties for S-type asteroids (Huang et al. 2017) adopted by the mutual event model may need to be revised.

We have also presented a simple phase curve analysis based on nightly average magnitudes from a few select observatories (Figure 8). This analysis showed that canonical  $HG$  magnitude predictions (Bowell et al. 1989) do not represent the data well, particularly at phase angles  $>40^\circ$ . An  $HG_1G_2$  model (Muinonen et al. 2010) does reproduce the data reasonably well with parameters adopted from Hasselmann (2023). However, the parameters used in this  $HG_1G_2$  model are unusual for S-type asteroids (Penttilä et al. 2016; Mahlke et al. 2021). These issues could be related to differences in the times and viewing geometries of our data relative to those used to derive the model parameters. Disentangling the effects of shape and viewing geometry on photometric phase curves can be challenging for near-Earth asteroids (e.g., Jackson et al. 2022). Further work is needed to address whether discrepancies with the mutual event model (e.g., Figure 7) could be attributed to these potentially unusual photometric properties of the Didymos system.

Lastly, we noted that all of our postimpact lightcurve photometry was performed in the presence of an ejecta cloud (for several weeks after impact) and a persistent tail that was still detectable 5 months after impact. We showed that by 1 month after impact, dust in the tail contributed  $<1\%$  of the nuclear signal and thus dropped below typical photometric error bars.

While the data and analysis presented here have contributed to successful completion of the DART mission's level 1 requirements (Chabot et al. 2023), open questions remain related to the photometric behavior of Didymos in the months after impact, the detailed morphology of mutual events, the role that ejecta played in the observed properties of the system, and the extent to which higher-order dynamical effects are detectable in these data. Fortunately, a number of these questions will be resolved when the European Space Agency's Hera mission arrives in the Didymos system in late 2026 (Michel et al. 2022). Hera, in its nominal mission, will rendezvous with Didymos and Dimorphos for a 6 month

investigation of surface and interior properties, as well as studies of any residual impact ejecta that may still be present in the system. Until then, ground-based observing opportunities in 2024 and 2025 will continue to provide deeper understanding of the post-DART Didymos system.

### Acknowledgments

This work is based upon a large volume of data collected at dozens of observatories around the world. We are deeply grateful to all of the telescope operators, engineers, instrument scientists, and site managers who enabled these observations. We acknowledge the thoughtful reviews provided by two anonymous referees.

Significant portions of this work were completed at Lowell Observatory, which sits at the base of mountains sacred to tribes throughout the region. We honor their past, present, and future generations, who have lived here for millennia and will forever call this place home.

Much of this work were supported by the DART mission under NASA contract No. 80MSFC20D0004. N.M. and T.K. acknowledge additional funding from NASA grants 80NSSC21K1328 and NNX17AH06G, awarded in support of the Mission Accessible Near-Earth Object Survey (MANOS). The work at Ondřejov and observations with the Danish telescope on La Silla were supported by the Grant Agency of the Czech Republic, grants 20-04431S and 23-4946S. Access to computing and storage facilities owned by parties and projects contributing to the National Grid Infrastructure MetaCentrum provided under the program “Projects of Large Research, Development, and Innovations Infrastructures” (CESNET LM2015042) and the CERIT Scientific Cloud LM2015085 is greatly appreciated. Y.K. is thankful for support from the European Federation of Academies of Sciences and Humanities (grant ALLEA EFDS-FL1-18). I.R. was funded by the Aerospace Committee of the Ministry of Digital Development, Innovations and Aerospace Industry of the Republic of Kazakhstan (grant No. BR 11265408). Y.K., O.B., and K.E. are grateful to the staff of the Maidanak Observatory for their support during the observations. A.R. and C.S. acknowledge support from the UK Science and Technology Facilities Council. This project has received funding from the European Union’s Horizon 2020 research and innovation program under grant agreement No. 870403 (NEOROCKS). P.L.P. was partly funded by the Programa de Iniciación en Investigación-Universidad de Antofagasta INI-17-03. The work of M.H. was supported by the Slovak Grant Agency for Science VEGA (grant No. 2/0059/22) and the Slovak Research and Development Agency under contract No. APVV-19-0072. T.S.R. acknowledges funding from the Ministerio de Ciencia e Innovación (Spanish Government), PGC2021, PID2021-125883NB-C21. This work was (partially) supported by the Spanish MICIN/AEI/10.13039/501100011033 and by “ERDF A way of making Europe” by the European Union through grant PID2021-122842OB-C21 and the Institute of Cosmos Sciences University of Barcelona (ICCUB, Unidad de Excelencia ‘María de Maeztu’) through grant CEX2019-000918-M. The work of M.P. and D.B. was supported by a grant of the Romanian National Authority for Scientific Research—UEFISCDI, project No. PN-III-P2-2.1-PED-2021-3625.

These results made use of the Lowell Discovery Telescope (LDT) at Lowell Observatory. Lowell is a private, nonprofit

institution dedicated to astrophysical research and public appreciation of astronomy and operates the LDT in partnership with Boston University, the University of Maryland, the University of Toledo, Northern Arizona University, and Yale University. The Large Monolithic Imager was built by Lowell Observatory using funds provided by the National Science Foundation (AST-1005313). This work is based in part on observations obtained at the Southern Astrophysical Research (SOAR) telescope, which is a joint project of the Ministério da Ciência, Tecnologia e Inovações do Brasil (MCTI/LNA), the US National Science Foundation’s NOIRLab, the University of North Carolina at Chapel Hill (UNC), and Michigan State University (MSU). This research is based on observations made with the 1.0 m Jacobus Kapteyn Telescope at the Roque de los Muchachos Observatory on La Palma and the 0.8 m IAC80 telescope at the Teide Observatory on Tenerife. D.O. was supported by grant No. 2022/B/ST9/00267 from the National Science Center, Poland. V.T. was supported by the National Scholarship program of the Slovak Republic—academic year 2023/24. TRAPPIST is a project funded by the Belgian Fonds (National) de la Recherche Scientifique (F.R.S.-FNRS) under grant PDR T.0120.21. TRAPPIST-North is a project funded by the University of Liège, in collaboration with the Cadi Ayyad University of Marrakech (Morocco). E.J. is an F.R.S.-FNRS Senior Research Associate. This work has made use of data from the Asteroid Terrestrial-impact Last Alert System (ATLAS) project. ATLAS is primarily funded to search for near-Earth asteroids through NASA grants NN12AR55G, 80NSSC18K0284, and 80NSSC18K1575; by-products of the NEO search include images and catalogs from the survey area. The ATLAS science products have been made possible through the contributions of the University of Hawaii Institute for Astronomy, the Queen’s University Belfast, the Space Telescope Science Institute, and the South African Astronomical Observatory. This paper is based on observations made with the MuSCAT3 instrument, developed by the Astrobiology Center and under financial supports by JSPS KAKENHI (JP18H05439) and JST PRESTO (JPMJPR1775), at Faulkes Telescope North on Maui, Hawaii, operated by the Las Cumbres Observatory. This paper was partially based on observations obtained at the Bohyunsan Optical Astronomy Observatory (BOAO), which is operated by the Korea Astronomy and Space Science Institute (KASI).

*Facilities:* Magellan:Baade (IMACS), LDT (LMI), SOAR (Goodman), FTN (MuSCAT3), VATT, BOAO:1.8 m, Danish 1.54 m Telescope (DFOSC), Maidanak:1.5 m, Sanchez (MuSCAT2), Hall (NASA42), LCOGT (Sinistro), ING:Kapteyn, Swope, Spacewatch:0.9 m, OT:0.8 m (CAMELOT2), OO:0.65, TRAPPIST.

*Software:* astropy (Astropy Collaboration et al. 2013, 2018), SExtractor (Bertin & Arnouts 1996), Scamp (Bertin 2006), sbpy (Mommert et al. 2019), Photometry Pipeline (Mommert 2017), Tycho Tracker (Parrott 2020), astroquery (Ginsburg et al. 2019).

### Appendix Observational Details

Here we provide a summary of observational circumstances for each of the lightcurves included for analysis (Table A1).

**Table A1**  
Observational Details for Each Lightcurve Presented in This Work

Facility	UTC Start	JD Range	Duration (hr)	Data Points	Decomposition ID
6.5 m Magellan	2022-07-02T04:00	2459762.66699 – 2459762.94198	6.6	193	Pre-L1
4.1 m SOAR	2022-07-04T06:52	2459764.78643 – 2459764.94339	3.8	129	Pre-L1
4.1 m SOAR	2022-07-05T04:24	2459765.68348 – 2459765.94987	6.4	210	Pre-L1
4.3 m LDT	2022-07-06T08:02	2459766.83477 – 2459766.96810	3.2	89	Pre-L1
4.3 m LDT	2022-07-07T07:50	2459767.82686 – 2459767.97285	3.5	85	Pre-L1
1 m LCOGT	2022-07-31T03:36	2459791.65044 – 2459791.90579	6.1	125	Pre-L2
1 m JKT	2022-08-18T00:45	2459809.53134 – 2459809.71404	4.4	119	Pre-L3.1
1 m JKT	2022-08-19T00:49	2459810.53460 – 2459810.71368	4.3	110	Pre-L3.1
1 m Swope	2022-08-22T01:37	2459813.56770 – 2459813.91689	8.4	498	Pre-L3.2
1 m Swope	2022-08-23T01:25	2459814.55946 – 2459814.92080	8.7	517	Pre-L3.2
0.7 m AC-32	2022-08-23T20:32	2459815.35618 – 2459815.55030	4.7	88	Pre-L3.2
1 m Swope	2022-08-24T01:29	2459815.56200 – 2459815.92027	8.6	518	Pre-L3.2
0.7 m AC-32	2022-08-24T21:09	2459816.38131 – 2459816.54553	3.9	82	Pre-L3.2
1 m Swope	2022-08-25T03:27	2459816.64420 – 2459816.91983	6.6	397	Pre-L3.2
0.7 m AC-32	2022-08-25T22:55	2459817.45536 – 2459817.54141	2.1	36	Pre-L3.2
1 m Swope	2022-08-30T00:51	2459821.53574 – 2459821.91384	9.1	531	Pre-L3.3
1 m Swope	2022-08-31T00:53	2459822.53737 – 2459822.91240	9.0	534	Pre-L3.3
1 m Swope	2022-09-01T01:00	2459823.54167 – 2459823.91311	8.9	523	Pre-L3.3
1 m Swope	2022-09-02T00:49	2459824.53435 – 2459824.91263	9.1	550	Pre-L3.3
0.6 m TS	2022-09-04T02:23	2459826.59957 – 2459826.86723	6.4	153	Pre-L3.4
0.6 m TS	2022-09-05T02:22	2459827.59877 – 2459827.69795	2.4	81	Pre-L3.4
0.6 m TS	2022-09-06T02:33	2459828.60646 – 2459828.67713	1.7	52	Pre-L3.4
0.6 m TS	2022-09-12T01:31	2459834.56367 – 2459834.74939	4.5	256	Pre-L4.1
1 m LCOGT	2022-09-12T14:10	2459835.09086 – 2459835.27470	4.4	198	Pre-L4.1
1 m LCOGT	2022-09-12T20:01	2459835.33419 – 2459835.51788	4.4	187	Pre-L4.1
0.6 m TS	2022-09-14T06:33	2459836.77356 – 2459836.90962	3.3	147	Pre-L4.1
0.6 m TS	2022-09-15T04:34	2459837.69065 – 2459837.81569	3.0	145	Pre-L4.1
1.5 m Danish	2022-09-16T08:22	2459838.84882 – 2459838.91024	1.5	98	Pre-L4.1
0.6 m TS	2022-09-18T07:49	2459840.82589 – 2459840.90635	1.9	76	Pre-L4.2
0.5 m T72	2022-09-20T01:44	2459842.57286 – 2459842.74630	4.2	162	Pre-L4.2
1.5 m Danish	2022-09-20T02:38	2459842.61009 – 2459842.90694	7.1	463	Pre-L4.2
0.6 m TS	2022-09-20T02:46	2459842.61532 – 2459842.70663	2.2	120	Pre-L4.2
0.6 m TS	2022-09-20T07:16	2459842.80324 – 2459842.90456	2.4	139	Pre-L4.2
0.6 m TS	2022-09-21T03:46	2459843.65757 – 2459843.90548	5.9	243	Pre-L4.2
0.6 m TS	2022-09-22T08:53	2459844.87053 – 2459844.90641	0.9	45	Pre-L4.2
0.6 m TS	2022-09-23T06:47	2459845.78307 – 2459845.90582	2.9	161	Pre-L4.3
0.6 m TS	2022-09-24T02:03	2459846.58601 – 2459846.89954	7.5	264	Pre-L4.3
0.6 m TS	2022-09-25T02:11	2459847.59151 – 2459847.89606	7.3	375	Pre-L4.3
1 m Swope	2022-09-25T03:16	2459847.63677 – 2459847.89319	6.2	435	Pre-L4.3
1.5 m Danish	2022-09-25T03:28	2459847.64511 – 2459847.89944	6.1	569	Pre-L4.3
1 m LCOGT	2022-09-25T14:50	2459848.11830 – 2459848.24055	2.9	172	Pre-L4.3
1.5 m Danish	2022-09-26T03:50	2459848.66035 – 2459848.70365	1.0	92	Pre-L4.3
1 m Swope	2022-09-26T02:15	2459848.59377 – 2459848.88760	7.1	429	Pre-L4.3
0.6 m TS	2022-09-26T07:41	2459848.82069 – 2459848.89597	1.8	113	Pre-L4.3
1 m Swope	2022-09-28T02:33	2459850.60635 – 2459850.75643	3.6	237	L0.1
1.5 m Danish	2022-09-28T02:38	2459850.60989 – 2459850.88674	6.6	340	L0.1
1 m Swope	2022-09-29T02:40	2459851.61163 – 2459851.88686	6.6	433	L0.2
1.5 m Danish	2022-09-29T02:50	2459851.61825 – 2459851.89795	6.7	639	L0.2
1 m LCOGT	2022-09-29T04:52	2459851.70320 – 2459851.86630	3.9	212	L0.2
0.6 m TN	2022-09-30T02:09	2459852.58974 – 2459852.72890	3.3	94	L0.3
1.5 m Danish	2022-09-30T02:40	2459852.61163 – 2459852.90395	7.0	669	L0.3
1 m Swope	2022-09-30T02:52	2459852.61965 – 2459852.88542	6.4	420	L0.3
1.5 m TCS	2022-09-30T03:36	2459852.65033 – 2459852.73971	2.1	86	L0.3
1 m LCOGT	2022-09-30T03:52	2459852.66165 – 2459852.88666	5.4	319	L0.3
0.6 m TS	2022-09-30T07:03	2459852.79385 – 2459852.88887	2.3	87	L0.3
1 m LCOGT	2022-09-30T21:45	2459853.40690 – 2459853.55059	3.4	168	L0.4
1 m Swope	2022-10-01T03:28	2459853.64455 – 2459853.88504	5.8	376	L0.4



**Table A1**  
(Continued)

Facility	UTC Start	JD Range	Duration (hr)	Data Points	Decomposition ID
0.6 m TS	2022-10-01T03:29	2459853.64552 – 2459853.88815	5.8	246	L0.4
1 m LCOGT	2022-10-01T04:00	2459853.66732 – 2459853.88294	5.2	292	L0.4
1.5 m Danish	2022-10-01T06:33	2459853.77308 – 2459853.89512	2.9	278	L0.4
1 m LCOGT	2022-10-01T21:48	2459854.40896 – 2459854.63187	5.3	268	L0.5
1.5 m Danish	2022-10-02T03:05	2459854.62906 – 2459854.85671	5.5	530	L0.5
1 m Swope	2022-10-02T03:15	2459854.63565 – 2459854.88820	6.1	396	L0.5
1 m LCOGT	2022-10-02T04:00	2459854.66735 – 2459854.88319	5.2	269	L0.5
1.1 m Hall	2022-10-02T08:19	2459854.84674 – 2459854.95490	2.6	132	L0.5
1 m LCOGT	2022-10-02T22:00	2459855.41728 – 2459855.53916	2.9	136	L0.6
1 m LCOGT	2022-10-03T01:00	2459855.54228 – 2459855.62661	2.0	99	L0.6
1 m Swope	2022-10-03T03:29	2459855.64571 – 2459855.89431	6.0	385	L0.6
0.6 m TS	2022-10-03T03:33	2459855.64845 – 2459855.87218	5.4	275	L0.6
1 m LCOGT	2022-10-03T04:05	2459855.67017 – 2459855.86302	4.6	248	L0.6
1.5 m Danish	2022-10-03T04:27	2459855.68573 – 2459855.72804	1.0	98	L0.6
0.6 m TN	2022-10-04T02:13	2459856.59250 – 2459856.70134	2.6	93	L0.7
0.6 m TS	2022-10-04T03:43	2459856.65517 – 2459856.86429	5.0	92	L0.7
1 m Swope	2022-10-04T03:46	2459856.65705 – 2459856.85069	4.6	224	L0.7
1 m LCOGT	2022-10-04T04:15	2459856.67770 – 2459856.86631	4.5	248	L0.7
1 m LCOGT	2022-10-04T23:15	2459857.46932 – 2459857.62841	3.8	206	L0.8
1.5 m Danish	2022-10-05T03:40	2459857.65293 – 2459857.74436	2.2	151	L0.8
0.6 m TS	2022-10-05T03:47	2459857.65778 – 2459857.74651	2.1	94	L0.8
1.1 m Hall	2022-10-05T08:03	2459857.83609 – 2459858.00200	4.0	142	L0.8
1 m Swope	2022-10-05T03:45	2459857.65664 – 2459857.77734	2.9	181	L0.8
1 m LCOGT	2022-10-05T22:18	2459858.42973 – 2459858.58280	3.7	194	L0.9
1 m Swope	2022-10-06T03:49	2459858.65972 – 2459858.88938	5.5	346	L0.9
1 m LCOGT	2022-10-06T04:31	2459858.68822 – 2459858.83991	3.6	194	L0.9
1.5 m Danish	2022-10-06T05:03	2459858.71052 – 2459858.89416	4.4	370	L0.9
0.6 m TS	2022-10-06T05:16	2459858.71951 – 2459858.85093	3.2	110	L0.9
1.5 m Danish	2022-10-07T04:10	2459859.67378 – 2459859.85302	4.3	379	L0.10
1.5 m TCS	2022-10-07T02:49	2459859.61755 – 2459859.75465	3.3	114	L0.10
1 m LCOGT	2022-10-07T04:52	2459859.70316 – 2459859.88078	4.3	219	L0.10
1 m LCOGT	2022-10-07T22:31	2459860.43826 – 2459860.62727	4.5	246	L0.11
0.6 m TS	2022-10-08T03:52	2459860.66117 – 2459860.73576	1.8	88	L0.11
1.5 m Danish	2022-10-08T04:00	2459860.66732 – 2459860.89540	5.5	471	L0.11
1 m LCOGT	2022-10-08T22:37	2459861.44249 – 2459861.62691	4.4	200	L0.12
0.6 m TS	2022-10-09T04:08	2459861.67266 – 2459861.86428	4.6	165	L0.12
1 m LCOGT	2022-10-09T04:49	2459861.70073 – 2459861.88372	4.4	244	L0.12
1.5 m Danish	2022-10-09T06:41	2459861.77911 – 2459861.89363	2.7	244	L0.12
0.6 m TS	2022-10-10T04:13	2459862.67614 – 2459862.86424	4.5	246	L0.13
1.5 m Danish	2022-10-10T04:30	2459862.68801 – 2459862.88784	4.8	419	L0.13
1 m LCOGT	2022-10-10T04:49	2459862.70070 – 2459862.79332	2.2	102	L0.13
1.5 m TCS	2022-10-17T02:50	2459869.61814 – 2459869.75936	3.4	114	L1.1
0.9 m Spacewatch	2022-10-17T10:43	2459869.94658 – 2459870.02078	1.8	51	L1.1
0.9 m Spacewatch	2022-10-20T09:01	2459872.87591 – 2459873.00474	3.1	92	L1.2
2.4 m MRO	2022-10-21T08:27	2459873.85238 – 2459873.99883	3.5	202	L1.2
0.9 m Spacewatch	2022-10-21T08:40	2459873.86150 – 2459874.01733	3.7	81	L1.2
1.1 m Hall	2022-10-24T08:06	2459876.83777 – 2459877.00597	4.0	81	L1.3
1.1 m Hall	2022-10-25T08:04	2459877.83659 – 2459878.00060	3.9	88	L1.3
0.9 m Spacewatch	2022-10-25T09:36	2459877.90001 – 2459878.01528	2.8	72	L1.3
1.1 m Hall	2022-10-26T08:05	2459878.83737 – 2459878.99494	3.8	91	L1.3
1.8 m VATT	2022-10-26T09:01	2459878.87629 – 2459879.01152	3.2	114	L1.3
0.9 m Spacewatch	2022-10-26T09:43	2459878.90541 – 2459879.01919	2.7	57	L1.3
1.1 m Hall	2022-10-27T08:00	2459879.83398 – 2459880.00799	4.2	94	L1.3
0.9 m Spacewatch	2022-10-27T10:20	2459879.93084 – 2459880.02873	2.3	69	L1.3
0.6 m Ondřejov	2022-10-28T00:59	2459880.54132 – 2459880.68111	3.4	94	L1.4
1 m LCOGT	2022-10-28T02:21	2459880.59792 – 2459880.75474	3.8	162	L1.4

**Table A1**  
(Continued)

Facility	UTC Start	JD Range	Duration (hr)	Data Points	Decomposition ID
0.6 m TS	2022-10-28T05:45	2459880.73984 – 2459880.87327	3.2	56	L1.4
1.5 m Danish	2022-10-29T07:18	2459881.80431 – 2459881.87030	1.6	69	L1.4
1.1 m Hall	2022-10-28T07:58	2459880.83197 – 2459881.01225	4.3	120	L1.4
1.1 m Hall	2022-10-29T07:50	2459881.82682 – 2459882.01607	4.5	110	L1.4
1.8 m VATT	2022-10-29T08:49	2459881.86752 – 2459882.02402	3.8	100	L1.4
1 m LCOGT	2022-10-30T02:16	2459882.59474 – 2459882.75793	3.9	178	L1.4
0.6 m Ondřejov	2022-10-30T02:20	2459882.59771 – 2459882.68875	2.2	36	L1.4
1.5 m Danish	2022-10-30T05:16	2459882.71997 – 2459882.86674	3.5	151	L1.4
1.1 m Hall	2022-10-31T07:47	2459883.82451 – 2459883.99910	4.2	124	L1.4
1.5 m Danish	2022-11-01T05:24	2459884.72555 – 2459884.86775	3.4	94	L1.4
1.5 m Danish	2022-11-02T05:27	2459885.72764 – 2459885.86534	3.3	92	L1.4
0.9 m Spacewatch	2022-11-02T09:27	2459885.89397 – 2459886.01292	2.9	69	L1.4
1.5 m TCS	2022-11-17T04:56	2459900.70591 – 2459900.77040	1.5	37	L2.1
4.3 m LDT	2022-11-17T07:24	2459900.80843 – 2459901.05212	5.8	379	L2.1
0.6 m TN	2022-11-18T01:04	2459901.54456 – 2459901.75044	4.9	125	L2.1
1 m LCOGT	2022-11-18T01:31	2459901.56323 – 2459901.75770	4.7	174	L2.1
4.3 m LDT	2022-11-18T07:26	2459901.81037 – 2459902.05936	6.0	479	L2.2
0.9 m Spacewatch	2022-11-19T08:34	2459902.85749 – 2459903.03832	4.3	113	L2.2
1.1 m Hall	2022-11-19T09:18	2459902.88771 – 2459903.02975	3.4	52	L2.2
0.6 m TN	2022-11-20T01:04	2459903.54492 – 2459903.74612	4.8	87	L2.2
1.1 m Hall	2022-11-20T06:47	2459903.78303 – 2459904.04012	6.2	108	L2.2
0.9 m Spacewatch	2022-11-20T07:41	2459903.82040 – 2459904.03469	5.1	147	L2.2
0.6 m TN	2022-11-21T01:48	2459904.57533 – 2459904.74878	4.2	103	L2.3
1.5 m Danish	2022-11-21T05:16	2459904.71981 – 2459904.86194	3.4	77	L2.3
1.1 m Hall	2022-11-21T06:42	2459904.77930 – 2459905.03178	6.1	104	L2.3
0.9 m Spacewatch	2022-11-21T09:03	2459904.87735 – 2459905.02906	3.6	103	L2.3
1.5 m Danish	2022-11-22T05:15	2459905.71932 – 2459905.85242	3.2	86	L2.3
1 m LCOGT	2022-11-22T01:16	2459905.55338 – 2459905.76103	5.0	159	L2.3
2.4 m MRO	2022-11-22T06:02	2459905.75173 – 2459905.91849	4.0	229	L2.3
1.1 m Hall	2022-11-22T06:35	2459905.77496 – 2459905.85868	2.0	39	L2.3
1.1 m Hall	2022-11-23T06:29	2459906.77020 – 2459907.04413	6.6	123	L2.3
1.5 m Danish	2022-11-24T05:12	2459907.71703 – 2459907.85243	3.2	77	L2.4
1.1 m Hall	2022-11-24T06:24	2459907.76714 – 2459908.03644	6.5	111	L2.4
0.9 m Spacewatch	2022-11-24T07:43	2459907.82161 – 2459908.04074	5.3	124	L2.4
1.5 m AZT-22	2022-11-24T20:49	2459908.36785 – 2459908.44936	2.0	76	L2.4
1 m LCOGT	2022-11-25T01:01	2459908.54258 – 2459908.76786	5.4	166	L2.4
1.1 m Hall	2022-11-25T06:30	2459908.77131 – 2459909.04076	6.5	117	L2.4
1.5 m Danish	2022-11-25T06:39	2459908.77729 – 2459908.85502	1.9	47	L2.4
0.9 m Spacewatch	2022-11-25T08:28	2459908.85347 – 2459909.03805	4.4	99	L2.4
1.5 m Danish	2022-11-26T05:56	2459909.74773 – 2459909.85536	2.6	47	L2.5
1.1 m Hall	2022-11-26T06:14	2459909.76004 – 2459910.04018	6.7	100	L2.5
1.5 m Danish	2022-11-27T05:36	2459910.73347 – 2459910.85399	2.9	61	L2.5
1.1 m Hall	2022-11-27T06:09	2459910.75637 – 2459911.04136	6.8	125	L2.5
1.5 m AZT-22	2022-11-27T19:24	2459911.30869 – 2459911.55133	5.8	160	L2.5
0.6 m Ondřejov	2022-11-27T22:02	2459911.41807 – 2459911.53662	2.8	44	L2.6
1.5 m Danish	2022-11-28T05:36	2459911.73380 – 2459911.78206	1.2	28	L2.6
0.6 m Stará Lesná	2022-11-28T23:27	2459912.47749 – 2459912.63264	3.7	58	L2.6
1.1 m Hall	2022-11-29T06:05	2459912.75399 – 2459913.01913	6.4	117	L2.6
1 m LCOGT	2022-11-30T00:51	2459913.53587 – 2459913.76175	5.4	162	L2.6
1.5 m Danish	2022-11-30T04:54	2459913.70480 – 2459913.85738	3.7	78	L2.6
1.1 m Hall	2022-11-30T06:03	2459913.75269 – 2459914.04306	7.0	114	L2.6
2.4 m MRO	2022-11-30T06:19	2459913.76355 – 2459913.99664	5.6	353	L2.6
0.9 m Spacewatch	2022-11-30T06:54	2459913.78763 – 2459914.03500	5.9	133	L2.6
1 m LCOGT	2022-11-30T06:50	2459913.78537 – 2459913.90697	2.9	89	L2.6
1 m LCOGT	2022-12-01T02:46	2459914.61557 – 2459914.74010	3.0	88	L2.7
1.1 m Hall	2022-12-01T05:48	2459914.74174 – 2459914.93801	4.7	82	L2.7
1.5 m Danish	2022-12-01T06:06	2459914.75456 – 2459914.85574	2.4	51	L2.7
2.4 m MRO	2022-12-01T06:15	2459914.76075 – 2459914.97346	5.1	240	L2.7
0.9 m Spacewatch	2022-12-01T07:13	2459914.80119 – 2459915.02296	5.3	142	L2.7
0.5 m Sugarloaf	2022-12-02T05:32	2459915.73117 – 2459915.94429	5.1	44	L2.7

**Table A1**  
(Continued)

Facility	UTC Start	JD Range	Duration (hr)	Data Points	Decomposition ID
2 m FTN	2022-12-14T10:02	2459927.91809 – 2459928.13465	5.2	249	L3.1
4.3 m LDT	2022-12-15T07:06	2459928.79595 – 2459929.06886	6.5	488	L3.1
1 m LCOGT	2022-12-16T23:41	2459930.48726 – 2459930.65677	4.1	116	L3.2
1.5 m Danish	2022-12-17T04:07	2459930.67167 – 2459930.85421	4.4	64	L3.2
1.1 m Hall	2022-12-17T04:23	2459930.68277 – 2459931.02634	8.2	120	L3.2
0.6 m TN	2022-12-18T22:18	2459932.42977 – 2459932.72830	7.2	139	L3.3
1.5 m Danish	2022-12-19T03:42	2459932.65464 – 2459932.85511	4.8	120	L3.3
1.1 m Hall	2022-12-19T04:10	2459932.67420 – 2459933.00020	7.8	128	L3.3
1 m Tien-Shan	2022-12-19T16:09	2459933.17361 – 2459933.43726	6.3	148	L3.3
1.5 m Danish	2022-12-20T03:54	2459933.66318 – 2459933.82730	3.9	79	L3.3
0.8 m IAC80	2022-12-20T04:05	2459933.67079 – 2459933.79256	2.9	46	L3.3
1.1 m Hall	2022-12-20T04:51	2459933.70215 – 2459933.83654	3.2	58	L3.3
0.6 m TN	2022-12-21T00:01	2459934.50107 – 2459934.64302	3.4	73	L3.3
1.1 m Hall	2022-12-21T04:15	2459934.67758 – 2459934.99702	7.7	117	L3.3
0.5 m Sugarloaf	2022-12-21T04:06	2459934.6710 3– 2459934.95380	6.8	127	L3.3
0.7 m AC-32	2022-12-21T18:51	2459935.28582 – 2459935.60357	7.6	120	L3.4
1.5 m Danish	2022-12-22T03:31	2459935.64693 – 2459935.85438	5.0	115	L3.4
1.5 m Danish	2022-12-23T04:03	2459936.66886 – 2 459936.82079	3.6	86	L3.4
0.7 m AC-32	2022-12-23T17:49	2459937.24273 – 2459937.56234	7.7	127	L3.4
1.8 m BOAO	2022-12-24T14:05	2459938.08730 – 2459938.37919	7.0	129	L3.5
2.4 m MRO	2022-12-25T03:37	2459938.65106 – 2459938.98469	8.0	465	L3.5
1.1 m Hall	2022-12-25T04:20	2459938.68114 – 2459938.77319	2.2	39	L3.5
1.1 m Hall	2022-12-26T04:46	2459939.69905 – 2459939.99006	7.0	124	L3.5
0.5 m Sugarloaf	2022-12-25T03:36	2459938.65060 – 2459938.94060	7.0	32	L3.5
0.5 m Sugarloaf	2022-12-26T04:02	2459939.66866 – 2459939.94683	6.7	96	L3.5
1.8 m BOAO	2022-12-26T13:04	2459940.04469 – 2459940.36915	7.8	160	L3.5
0.6 m Ondřejov	2022-12-27T22:33	2459941.43962 – 2459941.62416	4.4	73	L3.6
1.5 m Danish	2022-12-30T02:53	2459943.62060 – 2459943.85782	5.7	141	L3.6
1.5 m Danish	2022-12-31T04:15	2459944.67764 – 2459944.85225	4.2	103	L3.6
1 m LCOGT	2022-12-31T06:16	2459944.76126 – 2459944.89522	3.2	98	L3.6
1.5 m Danish	2023-01-11T01:50	2459955.57649 – 2459955.81858	5.8	103	L4.1
1 m LCOGT	2023-01-14T05:46	2459958.74075 – 2459958.90387	3.9	67	L4.1
0.6 m TN	2023-01-15T00:13	2459959.50919 – 2459959.65642	3.5	73	L4.1
1.5 m Danish	2023-01-15T01:32	2459959.56451 – 2459959.80226	5.7	96	L4.1
1 m LCOGT	2023-01-16T07:23	2459960.80828 – 2459960.94995	3.4	64	L4.1
1.5 m Danish	2023-01-18T01:26	2459962.55987 – 2459962.79337	5.6	98	L4.1
1.5 m Danish	2023-01-24T01:02	2459968.54363 – 2459968.69672	3.7	55	L4.2
1 m LCOGT	2023-01-24T20:06	2459969.33776 – 2459969.58969	6.0	102	L4.2
4.3 m LDT	2023-01-25T02:08	2459969.58954 – 2459970.01919	10.3	218	L4.2
1 m LCOGT	2023-01-26T01:57	2459970.58135 – 2459970.80766	5.4	93	L4.2
1 m LCOGT	2023-01-26T21:19	2459971.38821 – 2459971.55048	3.9	72	L4.2
1.5 m Danish	2023-01-28T01:01	2459972.54294 – 2459972.76243	5.3	73	L4.2
2.4 m MRO	2023-01-28T01:45	2459972.57311 – 2459972.75924	4.5	169	L4.2
1.5 m Danish	2023-01-29T01:30	2459973.56271 – 2459973.76053	4.7	80	L4.2
2.4 m MRO	2023-01-29T02:19	2459973.59682 – 2459973.74686	3.6	116	L4.2
2.4 m MRO	2023-01-30T02:24	2459974.60024 – 2459974.74168	3.4	77	L4.2
2.4 m MRO	2023-02-11T01:42	2459986.57115 – 2459986.90646	8.0	255	L5.1
4.3 m LDT	2023-02-17T02:32	2459992.60565 – 2459992.93700	8.0	80	L5.2
2.4 m MRO	2023-02-17T07:06	2459992.79600 – 2459992.93543	3.3	44	L5.2
4.3 m LDT	2023-02-21T02:15	2459996.59395 – 2459996.85968	6.4	117	L5.2
2.4 m MRO	2023-02-25T03:21	2459000.63968 – 2460000.82854	4.5	255	L5.2


**Note.** Line breaks represent independent decompositions, as indicated by the Decomposition ID.

## ORCID iDs


Nicholas Moskovitz  <https://orcid.org/0000-0001-6765-6336>


Cristina Thomas  <https://orcid.org/0000-0003-3091-5757>

Petr Pravec  <https://orcid.org/0000-0001-8434-9776>


Tim Lister  <https://orcid.org/0000-0002-3818-7769>

David Osip  <https://orcid.org/0000-0003-0412-9664>

Theodore Kareta  <https://orcid.org/0000-0003-1008-7499>

Agata Rożek  <https://orcid.org/0000-0003-2341-2238>

Steven R. Chesley  <https://orcid.org/0000-0003-3240-6497>


Shantanu P. Naidu  <https://orcid.org/0000-0003-4439-7014>


Peter Scheirich  <https://orcid.org/0000-0001-8518-9532>

Brian Skiff  <https://orcid.org/0000-0001-5306-6220>

Colin Snodgrass  <https://orcid.org/0000-0001-9328-2905>

Matthew M. Knight  <https://orcid.org/0000-0003-2781-6897>


Andrew S. Rivkin  <https://orcid.org/0000-0002-9939-9976>

Nancy L. Chabot  <https://orcid.org/0000-0001-8628-3176>

Vova Ayvazian  <https://orcid.org/0000-0001-5549-5037>

Zouhair Benkhaldoun  <https://orcid.org/0000-0001-6285-9847>

Mariangela Bonavita  <https://orcid.org/0000-0002-7520-8389>


Melissa J. Brucker  <https://orcid.org/0000-0002-2079-179X>

Martin J. Burgdorf  <https://orcid.org/0000-0002-5854-4217>


Otabek Burkhonov  <https://orcid.org/0000-0003-1169-6763>


Brian Burt  <https://orcid.org/0000-0002-6423-0716>

Carlos Contreras  <https://orcid.org/0000-0001-6293-9062>


Joseph Chatelain  <https://orcid.org/0000-0002-1278-5998>


Young-Jun Choi  <https://orcid.org/0000-0001-6060-5851>

Julia de León  <https://orcid.org/0000-0002-0696-0411>


Kamoliddin Ergashev  <https://orcid.org/0000-0002-7521-1078>

Tony Farnham  <https://orcid.org/0000-0002-4767-9861>

Marin Ferrais  <https://orcid.org/0000-0002-0535-652X>

Stefan Geier  <https://orcid.org/0000-0001-9456-8358>

Edward Gomez  <https://orcid.org/0000-0001-5749-1507>

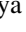
Sarah Greenstreet  <https://orcid.org/0000-0002-4439-1539>


Carrie Holt  <https://orcid.org/0000-0002-4043-6445>

Kamil Hornoch  <https://orcid.org/0000-0002-0835-225X>

Marek Husárik  <https://orcid.org/0000-0002-5932-7214>


Raguli Inasaridze  <https://orcid.org/0000-0002-6653-0915>


Emmanuel Jehin  <https://orcid.org/0000-0001-8923-488X>


Elahe Khalouei  <https://orcid.org/0000-0001-5098-4165>


Jean-Baptiste Kikwaya Eluo  <https://orcid.org/0000-0002-9502-2581>

Myung-Jin Kim  <https://orcid.org/0000-0002-4787-6769>


Yurij Krugly  <https://orcid.org/0000-0002-3171-9873>

Jeffrey A. Larsen  <https://orcid.org/0000-0002-0772-0225>

Hee-Jae Lee  <https://orcid.org/0000-0002-6839-075X>

Cassandra Lejoly  <https://orcid.org/0000-0003-0165-7701>

Javier Licandro  <https://orcid.org/0000-0002-9214-337X>

Penélope Longa-Peña  <https://orcid.org/0000-0001-9330-5003>

Curtis McCully  <https://orcid.org/0000-0001-5807-7893>

Hong-Kyu Moon  <https://orcid.org/0000-0001-5666-9967>

Nidia Morrell  <https://orcid.org/0000-0003-2535-3091>

Arushi Nath  <https://orcid.org/0009-0007-5329-9148>

Dagmara Oszkiewicz  <https://orcid.org/0000-0002-5356-6433>

Markus Rabus  <https://orcid.org/0000-0003-2935-7196>

Inna Reva  <https://orcid.org/0000-0001-9944-8398>

Audrey Thirouin  <https://orcid.org/0000-0002-1506-4248>

David Tholen  <https://orcid.org/0000-0003-0773-1888>

Volodymyr Troianskyi  <https://orcid.org/0000-0002-5899-2300>

## References

- Akhlaghi, M. 2019, arXiv:1909.11230
- Akhlaghi, M., & Ichikawa, T. 2015, *ApJS*, 220, 1
- Astropy Collaboration, Price-Whelan, A. M., Sipőcz, B. M., et al. 2018, *AJ*, 156, 123
- Astropy Collaboration, Robitaille, T. P., Tollerud, E. J., et al. 2013, *A&A*, 558, A33
- Bagnulo, S., Gray, Z., Granvik, M., et al. 2023, *ApJL*, 945, L38
- Barbary, K., 2018 SEP: Source Extraction and Photometry, Astrophysics Source Code Library, record ascl:1811.004
- Bertin, E. 2006, in ASP Conf. Ser. 351, Astronomical Data Analysis Software and Systems XV, ed. C. Gabriel et al. (San Francisco, CA: ASP), 112
- Bertin, E., & Arnouts, S. 1996, *A&AS*, 117, 393
- Bessell, M. S. 1990, *PASP*, 102, 1181
- Bowell, E., Hapke, B., Domingue, D., et al. 1989, in Asteroids II, ed. R. P. Binzel, T. Gehrels, & M. S. Matthews (Tucson, AZ: Univ. Arizona Press), 524
- Brown, T. M., Baliber, N., Bianco, F. B., et al. 2013, *PASP*, 125, 1031
- Chabot, N., Rivkin, A., Cheng, A., et al. 2023, *PSJ*, in press
- Cheng, A. F., Michel, P., Jutzi, M., et al. 2016, *P&SS*, 121, 27
- Clemens, J. C., Crain, J. A., & Anderson, R. 2004, *Proc. SPIE*, 5492, 331
- Collins, K. A., Kielkopf, J. F., Stassun, K. G., & Hessman, F. V. 2017, *AJ*, 153, 77
- Daly, R. T., Ernst, C. M., Barnouin, O. S., et al. 2023, *Natur*, 616, 443
- Dotto, E., Della Corte, V., Amoroso, M., et al. 2021, *P&SS*, 199, 105185
- Dotto, E., & Zinzi, A. 2023, *NatCo*, 14, 3055
- Dressler, A., Bigelow, B., Hare, T., et al. 2011, *PASP*, 123, 288
- Fahnstocck, E. G., Cheng, A. F., Ivanovski, S., et al. 2022, *PSJ*, 3, 206
- Fletcher, Z. J., Ryan, K. J., Maas, B. J., et al. 2018, *Proc. SPIE*, 10698, 106981X
- Flewelling, H. A., Magnier, E. A., Chambers, K. C., et al. 2020, *ApJS*, 251, 7
- Gaia Collaboration, Brown, A. G. A., Vallenari, A., et al. 2018, *A&A*, 616, A1
- Gaia Collaboration, Brown, A. G. A., Vallenari, A., et al. 2021, *A&A*, 649, A1
- Gilliland, R. L., & Brown, T. M. 1988, *PASP*, 100, 754
- Ginsburg, A., Sipőcz, B. M., Brasseur, C. E., et al. 2019, *AJ*, 157, 98
- Graykowski, A., Lambert, R. A., Marchis, F., et al. 2023, *Natur*, 616, 461
- Hasselmann, P., Dotto, E., Deshapriya, J. D. P., et al. 2023, *LPSC*, 54, 2023
- Hasselmann, P., Della Corte, V., Pravec, P., et al. 2023, *PSJ*, submitted
- Huang, X.-J., Lu, X.-P., Li, J.-Y., et al. 2017, *RAA*, 17, 106
- Im, M.-S., Ko, J.-W., Cho, Y.-S., et al. 2010, *JKAS*, 43, 75
- Jackson, S. L., Rozitis, B., Dover, L. R., et al. 2022, *MNRAS*, 513, 3076
- Jehin, E., Gillon, M., Quéloz, D., et al. 2011, *Msngr*, 145, 2
- Jester, S., Schneider, D. P., Richards, G. T., et al. 2005, *AJ*, 130, 873
- Jewitt, D., Kim, Y., Li, J., & Mutchler, M. 2023, *ApJL*, 952, L12
- Kaasalainen, M., & Torppa, J. 2001, *Icar*, 153, 24
- Kareta, T., Thomas, C. J.-Y. L., Knight, M., et al. 2023, *ApJL*, 959, L12
- Kelley, M., & Lister, T. 2022, *mkkelley/calviacat: v1.3.0*, Zenodo, doi:10.5281/zenodo.7019180
- Kitazato, K., Abe, M., Mito, H., et al. 2004, *LPSC*, 35, 1623
- Landolt, A. U. 1992, *AJ*, 104, 340
- Lister, T. A., Gomez, E., Chatelain, J., et al. 2021, *Icar*, 364, 114387
- Mahlke, M., Carry, B., & Denneau, L. 2021, *Icar*, 354, 114094
- McCully, C., Volgenau, N. H., Harbeck, D. R., et al. 2018, *Proc. SPIE*, 10707, 107070K
- Meyer, A. J., Gkolias, I., Gaitanas, M., et al. 2021, *PSJ*, 2, 242
- Michel, P., Küppers, M., Bagatin, A. C., et al. 2022, *PSJ*, 3, 160
- Mommert, M. 2017, *A&C*, 18, 47
- Mommert, M., Kelley, M., de Val-Borro, M., et al. 2019, *JOSS*, 4, 1426
- Moskovitz, N. A., Wasserman, L., Burt, B., et al. 2022, *A&C*, 41, 100661
- Mottola, S., De Angelis, G., Di Martino, M., et al. 1995, *Icar*, 117, 62
- Muñón, K., Belskaya, I. N., Cellino, A., et al. 2010, *Icar*, 209, 542
- Naidu, S., Chesley, S. R., Moskovitz, N., et al. 2023, *PSJ*, submitted
- Naidu, S. P., Benner, L. A. M., Brozovic, M., et al. 2020, *Icar*, 348, 113777
- Naidu, S. P., Chesley, S. R., Farnocchia, D., et al. 2022, *PSJ*, 3, 234
- Narita, N., Fukui, A., Kusakabe, N., et al. 2019, *JATIS*, 5, 015001
- Narita, N., Fukui, A., Yamamuro, T., et al. 2020, *Proc. SPIE*, 11447, 114475K
- Niels Bohr Institut Institut of Astronomy, CambridgeReal Instituto y Observatorio de La Armada 2014, *yCat*, 1/327, 0
- Oszkiewicz, D., Troianskyi, V., Föhning, D., et al. 2020, *A&A*, 643, A117
- Oszkiewicz, D., Troianskyi, V., Galád, A., et al. 2023, *Icar*, 397, 115520

- Oszkiewicz, D., Wilawer, E., Podlewska-Gaca, E., et al. 2021, *Icar*, **357**, 114158
- Parrott, D. 2020, *JAAVSO*, **48**, 262
- Penttilä, A., Shevchenko, V. G., Wilkman, O., & Muinonen, K. 2016, *P&SS*, **123**, 117
- Pravec, P., Benner, L. A. M., Nolan, M. C., et al. 2003, *IAUC*, **8244**, 2
- Pravec, P., Harris, A. W., Kušnirák, P., Galád, A., & Hornoch, K. 2012, *Icar*, **221**, 365
- Pravec, P., Scheirich, P., Kušnirák, P., et al. 2006, *Icar*, **181**, 63
- Pravec, P., Thomas, C. A., Rivkin, A. S., et al. 2022, *PSJ*, **3**, 175
- Pravec, P., Šarounová, L., Rabinowitz, D. L., et al. 2000, *Icar*, **146**, 190
- Rivkin, A. S., Chabot, N. L., Stickle, A. M., et al. 2021, *PSJ*, **2**, 173
- Sanchez, J. A., Reddy, V., Thirouin, A., et al. 2019, *ApJL*, **881**, L6
- Scheirich, P., & Pravec, P. 2022, *PSJ*, **3**, 163
- Scheirich, P., Pravec, P., Meyer, A. J., et al. 2024, *PSJ*, **5**, 17
- Stickle, A. M., DeCoster, M. E., Burger, C., et al. 2022, *PSJ*, **3**, 248
- Thomas, C. A., Naidu, S. P., Scheirich, P., et al. 2023, *Natur*, **616**, 448
- Tody, D. 1986, *Proc. SPIE*, **627**, 733
- Tonry, J. L., Denneau, L., Flewelling, H., et al. 2018, *ApJ*, **867**, 105
- Tonry, J. L., Stubbs, C. W., Lykke, K. R., et al. 2012, *ApJ*, **750**, 99